

# Design and Evaluation of Robust Control Methods for Robotic Transfemoral Prostheses

Nitish Thatte

March 9, 2019

The Robotics Institute  
Carnegie Mellon University  
Pittsburgh, PA 15213

*Thesis Committee:*

Hartmut Geyer (Chair)

Chris Atkeson

Aaron Johnson

Steven Collins, Stanford University

Elliott Rouse, University of Michigan

*Submitted in partial fulfillment of the requirements  
for the degree of Doctor of Philosophy*

Copyright ©2019 Nitish Thatte.



## *Contents*



*List of Figures*



*List of Tables*



# 1

## *Introduction*

### *1.1 Motivation*

SIX HUNDRED THOUSAND lower-limb amputees currently live in the United States according to recent estimates (?). People undergo amputations due to a variety of reasons including traumatic injuries from workplace accidents, traffic collisions, and as casualties of war. In addition, a large percentage (54%) suffer from the loss of a limb due to complications arising from dysvascular disease associated with diabetes. Consequently, largely due to the expected increase in diabetes in the coming years, ? estimate that by 2050 the number of amputees living in the United States will likely double.

Currently, prosthetists often prescribe transfemoral amputees (those with amputations between the hip and knee joints) an energy storage and return composite foot such as the Thrive Foot (Freedom Innovations; Irvine, CA; fig. 1.1c) along with a microprocessor-controlled, mechanically-passive knee prosthesis. These knee prostheses feature control algorithms that adjust the knee's resistance in response to kinematic and force data measured by sensors embedded in the device. Examples of microprocessor-controlled prosthetic knees include the C-Leg (Otto Bock; Duderstadt, Germany; fig. 1.1a), which has an adjustable hydraulic damping system, and the Rheo Knee (Össur; Reykjavik, Iceland; fig. 1.1b), which achieves variable damping via a magnetorheological fluid. While ? show these microprocessor-controlled knees can improve amputee gait characteristics by decreasing metabolic energy consumption and peak hip torque and increasing gait smoothness compared to that provided by fully-passive knee prosthesis, these prostheses still cannot fully replicate healthy leg behavior as they are incapable of providing positive net power during the gait cycle adn are may be limited to providing positive power only during fixed portions of the gait cycle.

Control of positive power generation is important as positive



(a) C-Leg™ Knee ©Ottobock



(b) Rheo™ Knee ©Össur



(c) Thrive™ Foot ©Freedom Innovations

Figure 1.1: Examples of microprocessor-controlled mechanically-passive knee prostheses (a,b) and a energy storage and return ankle-foot prosthesis (c).

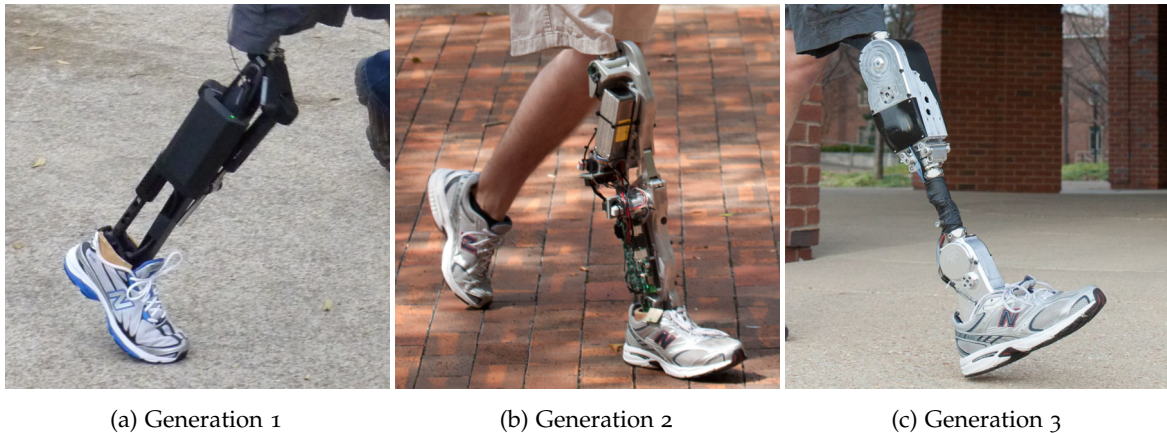
power is evident in a number of locomotion tasks. In the knee joint, we see positive power during level walking (?), walking up stairs (?), running (?), and jumping (?). In addition, active knee flexion and extension muscle activations have been noted during stumble recovery (?). At the ankle joint, passive spring-like prostheses cannot replicate the positive net work seen in the ankle joint during level ground walking, which is essential for push-off and forward propulsion (?).

Consequently, lower-limb amputees and especially *transfemoral amputees*, those with above the knee amputations, equipped with mechanically-passive prostheses suffer from a number of issues including markedly increased energy consumption (?), abnormal gait kinematics (?), and an increased likelihood of falling (?). Specifically, large percentages of transfemoral amputees report they are unable to complete tasks such as walking outside in inclement weather (47.4%), walking while carrying a load (42.7%), walking up or down stairs without a handrail (38.5%, 37.9%), walking outside on uneven terrain (29.5%), picking up an object from the ground (28.1%) or getting up from the floor after a fall (22.8%) (?).

Importantly, these gait pathologies can lead to an avoidance of walking (?). This is especially true in the case of falls. ? find 49.2% of lower limb amputees feared falling and that of those afraid of falls 76% avoided physical activity as a result. Avoidance of physical activity is eminently concerning as it may lead to reduced strength, endurance, and balance, feeding a positive feedback loop that causes further debilitation.

To help remedy this situation, in the past decade academic research groups and companies have developed robotic powered knee and ankle prostheses for lower-limb amputees. These prostheses feature actuators at the knee and/or ankle that, if controlled correctly, could potentially restore the kinetics, kinematics, and re-

Figure 1.2: Vanderbilt University's Robotic Transfemoral Prostheses. Images courtesy of Michael Goldfarb.



actions of the healthy human leg. Notable examples include three generations of transfemoral prostheses developed by Vanderbilt University (fig. 1.2) (???) and the Biom powered ankle (fig. 1.3) (?). These powered prostheses have helped amputees walk on level ground more naturally and efficiently, as well as walk up stairs and slopes (??), run (??), perform sit-to-stand (?), and dance (?). These results illustrate the benefits of powered prostheses as many of these tasks require positive joint power and thus would be difficult to perform with mechanically-passive prostheses.

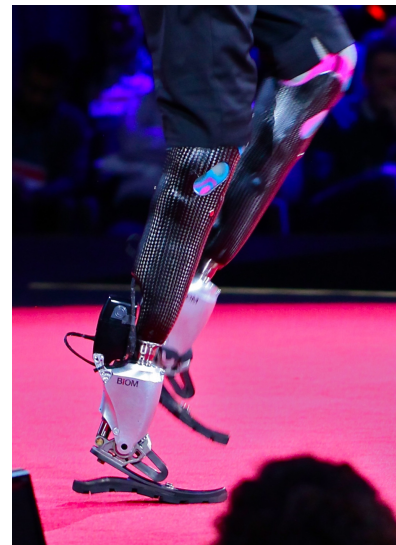


Figure 1.3: Biom Robotic Ankle Prosthesis. Photo by Steve Jurvetson, CC BY 2.0, Link (cropped from original).



## 2

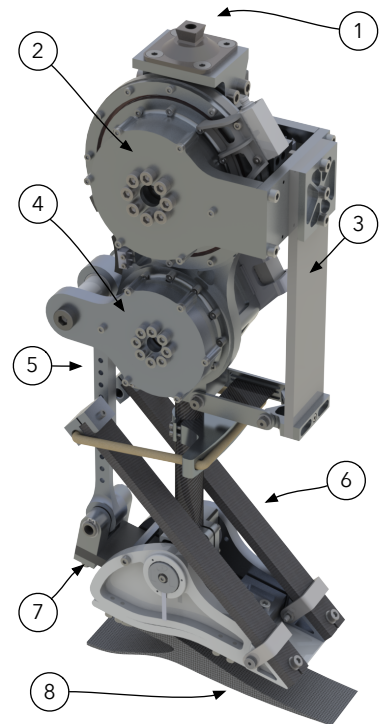
# *Transfemoral Prosthesis Development*

### *2.1 Mechanical Design*

TO TEST OUR PROPOSED NEUROMUSCULAR CONTROL APPROACH, and its ability to help subjects maintain or recover their balance, we build a custom transfemoral prosthesis capable of reproducing dynamic locomotion tasks. The proposed design, shown in fig. 2.1, uses brushless electric motors coupled to harmonic drive gear sets to drive both the knee and ankle joints. Additionally, the joints employ series elastic actuation to enable accurate torque control and to protect the prosthesis' gear sets from sudden impacts. The design also features a unidirectional parallel spring in the ankle that partly offsets the torque demands on the ankle motor. We design both joints to meet the demands of dynamic locomotion tasks such as running and trip recovery.

The overall design concept sits in a niche between low powered prostheses designed with commercial applicability in mind (?????) which feature onboard actuation and power sources, and high-powered tethered systems (??) with off-board actuation designed exclusively for use in lab environment. Our design features onboard actuators that are more powerful than those used in standalone devices, but less capable than those employed in tethered devices. To ensure a reasonable overall weight the device's batteries, motor drivers, and computers are off-board. With this design, we expect to be able to test control ideas without encountering hardware performance limitations as with a tethered device. At the same time the device is capable of functioning outside of the lab environment like a standalone prosthesis.

Table 2.1 shows the desired design specifications for the transfemoral prosthesis and the values achieved by the final design. To obtain these design specifications we examined a number of studies that elicited trip responses.



- 1) Pyramid Adaptor
- 2) Knee Motor
- 3) Knee Series Spring
- 4) Ankle Motor
- 5) Adjustable Height
- 6) Unidirectional Parallel Spring
- 7) Ankle Series Spring
- 8) Composite Foot

Figure 2.1: Render of proposed powered knee and ankle prosthesis design. The prosthesis includes series elastic actuators to enable accurate torque control and a unidirectional parallel ankle spring to offset the required angle torque.

Specification	Desired Value	Theoretical Value	Achieved Value
Maximum Knee Torque	160 N · m	170 N · m	
Maximum Knee Speed	1.80 rev/s	1.93 rev/sec	
Knee Torque Bandwidth	4 Hz	11.7 Hz	
Maximum Ankle Torque	200 N · m	170 (+120*) N · m	
Maximum Ankle Speed	1.14 rev/s	1.22 rev/s	
Ankle Torque Bandwidth	3.5 Hz	5.9 Hz	
Weight	6.8 kg	5.9 kg	
Minimum Height	42.5 cm	42 cm	

We specify desired joint torque and speed values to meet the requirements of demanding tasks such as running. The maximum knee torque specification comes from the findings of ?, who tested the joint torques used during recovery from a simulated fall. The maximum knee speed requirement comes from ?, who tested subjects' responses to simulated trips induced by unseen obstacles on a walkway. We obtain the maximum ankle torque requirement from ?, who tripped subjects using a obstacles that could suddenly emerge through the floor. The maximum ankle speed requirement comes from the running data of ?. We set to the minimum height specification, measured between the center of the knee and bottom of the foot, to accommodate the 10<sup>th</sup> percentile female (?). Finally, the required weight corresponds to the mean leg weight of a 50<sup>th</sup> percentile male (?).

### 2.1.1 Knee Joint

In addition to achieving the maximum speeds and torques found in table 2.1, we design the knee joint so that it can reproduce the torque and speed required for a 80 kg person to run at 3.2 m/s as measured by ?. To reproduce this trajectory in the knee joint, we utilize a RoboDrive ILM 85 × 13 HS-SP motor coupled to a Harmonic Drive Gear set with a 50:1 reduction (CSG-25-50). Figure 2.2 shows the motor torque and speed required to reproduce a running trajectory assuming a gear efficiency of 75%. In this plot, we see that the running trajectory lies within the speed-dependent torque limit of the motor. Moreover, the root mean squared torque of this trajectory (1.46 N · m) exceeds the torque rating of the motor (1.43 N · m) by just 2%. Therefore, the knee joint should be able to provide the necessary torque to enable running for a short amount of time, or continuously for lighter subjects or at a slightly reduced speed.

Figure 2.3 shows the internal and external design of the knee joint. The primary component in the knee joint is the stator housing. On

Table 2.1: Designed and achieved design specifications. (\*Maximum total ankle torque is 290 N · m achieved at 10 degrees of dorsiflexion.)

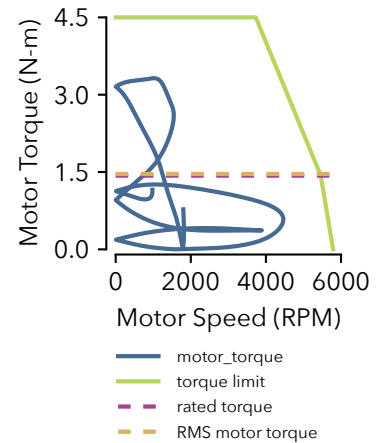
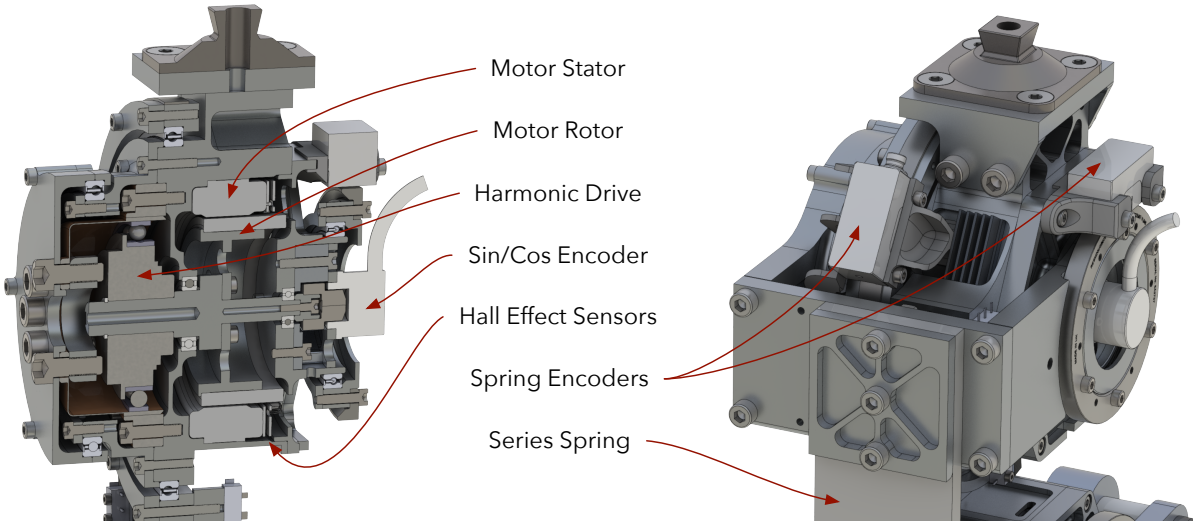


Figure 2.2: Knee motor torque required for running



top of the housing is a standard pyramid adaptor that allows the prosthesis to connect to amputee's sockets. Within the stator housing, lies the brushless motor stator, rotor, and harmonic drive gear set. We sense absolute rotor angle for commutation of the brushless motor via hall effect sensors and a magnetic complementary sin/cos encoder. To incorporate series elasticity, we take inspiration from the design of the bipedal robot Atrias (?), which uses fiberglass series leaf springs. In our design, the output of the gear set drives the proximal end of a fiberglass leaf spring in series with the shank. Two Renishaw Resolute absolute encoders measure the deflection of this spring to enable torque control.

In addition to allowing for accurate torque control, as shown by ??, the series elasticity also plays a crucial role in protecting fragile gear components from impact loads. To choose the spring stiffness for the knee joint, we simulate the prosthesis impacting a rigid wall with the foot during swing. To do this, we construct a model of the prosthesis in Matlab Simulink Simscape Multibody that includes the series elasticity, gear dynamics, and motor electrical dynamics. Figure 2.4 shows the simulation environment. The prosthesis is attached to the distal end of a thigh segment with a fixed hip position. We control the hip via the ideal swing leg control outlined in ?? (??) and consider the case where the external voltage applied to the motor is zero. This simulation suggests that a spring stiffness under  $2300 \text{ N}\cdot\text{m}/\text{rad}$  will ensure that the peak impact torque remains lower than the peak allowable impact torque of the Harmonic Drive of  $242 \text{ N}\cdot\text{m}$ .

We can also estimate the torque bandwidth of the actuator by analyzing the SEA dynamics for the system depicted in ???. Assuming

Figure 2.3: Internal and external design of the knee joint.

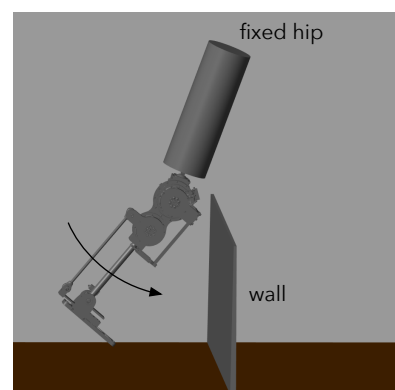


Figure 2.4: Impact simulation we used to determine appropriate series spring stiffness.

the load is fixed, the transfer function between the motor and load torques is given by

$$\frac{\tau_l}{\tau_m} = \frac{k/J_m}{s^2 + k/J_m} \quad (2.1)$$

where  $\tau_l$  and  $\tau_m$  are the load torque and post-gearbox motor torque respectively.  $J_m$  is the sum of the reflected motor rotor inertia and inertia of components that form the motor-side attachment of the spring, which has stiffness  $k$ . From this equation we calculate the bandwidth of the system to be

$$f_{3dB} = \frac{\sqrt{k/J_m}}{2\pi}. \quad (2.2)$$

For a spring stiffness of 2300 N·m/rad we estimate the torque bandwidth is 11.7 Hz. This value exceeds the required torque bandwidth of 4 Hz given by ? (obtained by analyzing the torque data for walking reported by ?). However, it should be noted that this is a very crude estimate of bandwidth. On the one hand, it may underestimate the true value, as it assumes that to achieve a desired output torque, the motor control applies the same torque to the motor side of the spring. In practice, a closed-loop torque control can transiently apply much larger torques to the motor side in order to achieve faster convergence to a desired steady-state output torque. On the other hand, this value may also underestimate the true bandwidth, as it does not consider the motor's voltage-current dynamics or gear friction.

### 2.1.2 Ankle Joint

In the ankle joint we utilize a RoboDrive ILM 70 × 10 HS-SP motor coupled to a Harmonic Drive Gear set with a 100:1 reduction (CSG-20–100). As with the knee joint, we design the ankle joint to satisfy the requirements listed in table 2.1. Specifically, for the ankle joint we pay considerable attention to the tripping condition described by ?, in which the ankle generates a peak torque of 202 N · m.

To avoid using a large and heavy motor to achieve this peak torque, we take inspiration from previous prosthetic ankle designs that employ a unidirectional parallel spring in the ankle joint that performs the conservative portion of the ankle's torque versus angle trajectory during normal walking (????). The parallel spring offsets the required motor torque, as the actuator only needs to provide the difference between the desired torque and the torque provided by the parallel spring. Figure 2.5 shows the torque versus angle curve during level ground walking (?), scaled to 80 kg person). In green we show the torque generated by a 700 N·m/rad parallel spring optimized to minimize the root-mean-squared motor torque for this trajectory.

From this plot, we see that with the parallel spring, the peak torque is lower than the repeated peak torque limit of the Harmonic Drive Gear set.

The tripping data obtained by ? shows that the ankle kinematics during trip recovery are similar to those seen during normal walking. Therefore, the parallel spring, should be able to contribute torque during the tripping case as well. To confirm this, fig. 2.6 shows the motor torque required for trip recovery (obtained by scaling walking torque data from ? to have a peak torque of  $202 \text{ N} \cdot \text{m}$ ) We see that the inclusion of the parallel spring allows the prosthesis to produce enough net torque to reproduce the trip recovery trajectory without exceeding the torque limit of the motor.

Finally, fig. 2.7 shows the torque and speed required of the motor for running (?). In this case, we use an ankle parallel stiffness of  $267 \text{ N} \cdot \text{m}/\text{rad}$ . From this plot, we see that this combination of ankle motor and spring is nearly sufficient for running. Increasing the voltage of the prosthesis from  $48 \text{ V}$  to  $60 \text{ V}$  or decreasing the gear ratio from  $100:1$  to  $80:1$  will allow the torque trajectory to fit completely within the motor limits.

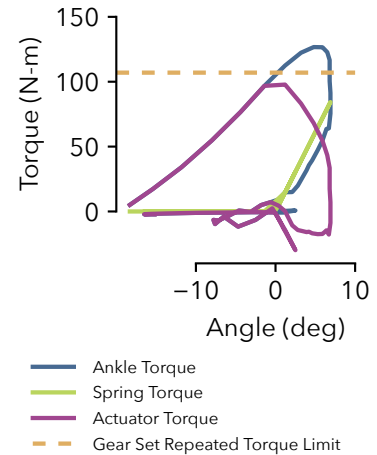


Figure 2.5: Ankle torque vs angle curve during steady, level-ground walking (blue) (?) scaled to  $80 \text{ kg}$  person). A unidirectional parallel spring can provide a portion of this torque (green) and reduces the required actuator torque (purple) to lie under repeated torque limit of the Harmonic Drive Gear set (orange).

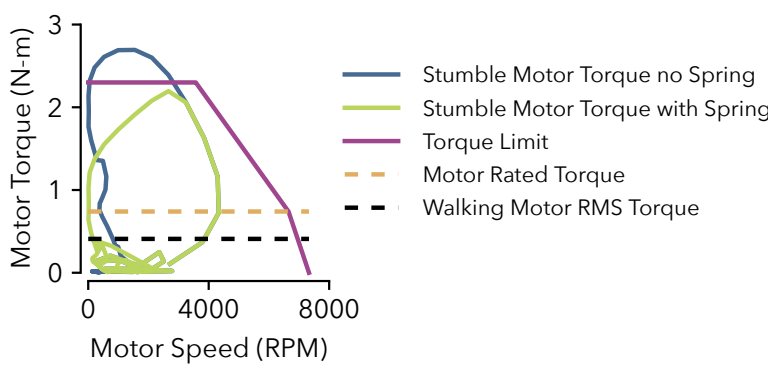


Figure 2.6: Ankle motor torque required to take the trip recovery action observed by ? (blue, trajectory obtained by scaling walking data from ? to a peak torque of  $202 \text{ N} \cdot \text{m}$ , 75% gear efficiency assumed). Using a parallel spring allows the motor to produce the required torque (green) while remaining within its torque limit (purple).

Figure 2.8 shows an internal view of the ankle actuator and external views of the actuator and foot mechanism. In the ankle design, the output of the actuator actuates the foot through a four-bar mechanism. The actuator pulls or pushes on the proximal end of a length-adjustable tendon. The distal end of the tendon attaches to one end of a fiberglass series elastic leaf spring that is also connected to the foot. By measuring the angles of the ankle actuator output and the ankle joint and using the equations of the four-bar mechanism's kinematics, we can calculate the deflection of the leaf spring and thus the torque applied to the ankle.

The design of the ankle actuator represents a second iteration of the knee actuator design and features two main improvements. First, it has increased space on the side of the motor for cable routing. Second, the ankle actuator has a solid rotor shaft. In contrast, the knee actuator's shaft is comprised of two parts: one that held the motor rotor and transferred power through the gear set, and another that held the sin/cos encoder's magnetic shaft component. In practice, these two components proved difficult to align, causing degraded performance of the sin/cos encoder. The ankle actuator's solid shaft ensures the encoder magnet stays aligned with the read head.

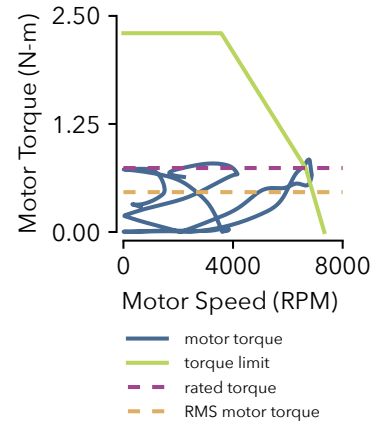


Figure 2.7: Ankle motor torque required to reproduce the running trajectory recorded by ? assuming a parallel spring stiffness of  $267 \text{ N}\cdot\text{m}/\text{rad}$  and a gear efficiency of 75%.

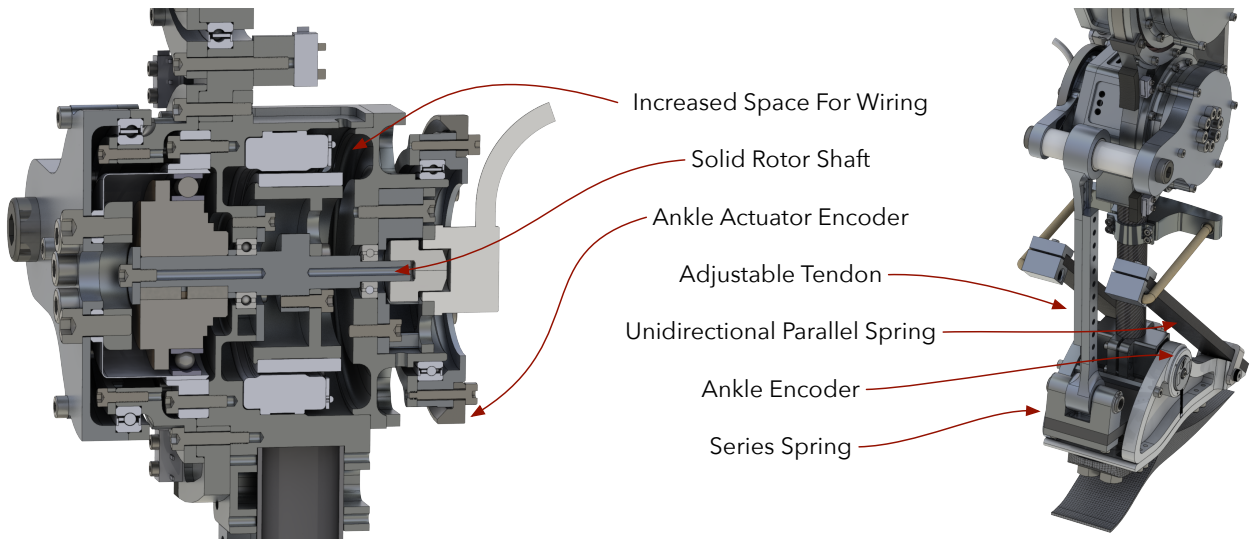


Figure 2.8: Internal and external design of the ankle joint.

As we did for the knee series spring, we again determine an acceptable ankle spring stiffness by performing an impact simulation. For the ankle, we simulate an 80 kg person stepping on the prosthesis when the motor driver provides the ankle motor with zero applied voltage. Figure 2.9 shows the simulation environment. From this simulation we find that a spring stiffness of about 1000 N·m/rad should sufficiently protect the ankle gear set from impacts. This estimate is likely softer than necessary due to the additional series compliance in the amputee's socket and the composite foot that are not included in the simulation. Repeating the bandwidth calculation we performed for the knee spring, we estimate the ankle bandwidth may be around 5.9 Hz. This value exceeds the required torque bandwidth of 3.5 Hz given by ? (obtained by analyzing the torque data for walking reported by ?).

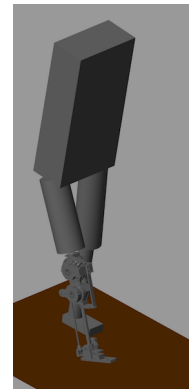
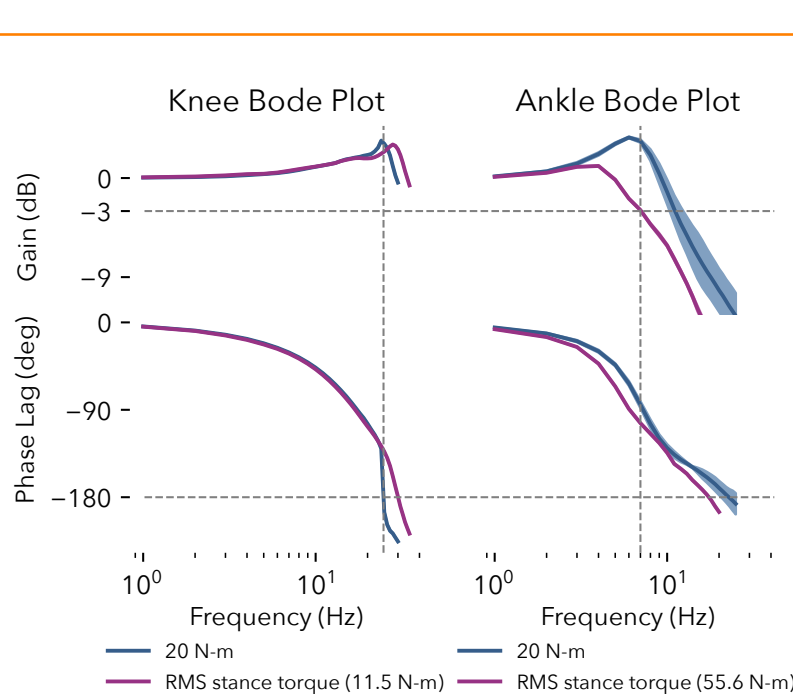


Figure 2.9: Impact simulation we used to determine appropriate series spring stiffness.

## 2.2 Performance Evaluation



Closeup of final design

Pictures of test rig

Figure 2.10: Experimentally obtained bode plots of knee and ankle actuator torque. Knee is phase limited at 24 Hz while the ankle is gain limited at 7 Hz.

torque tracking during walking RMS error

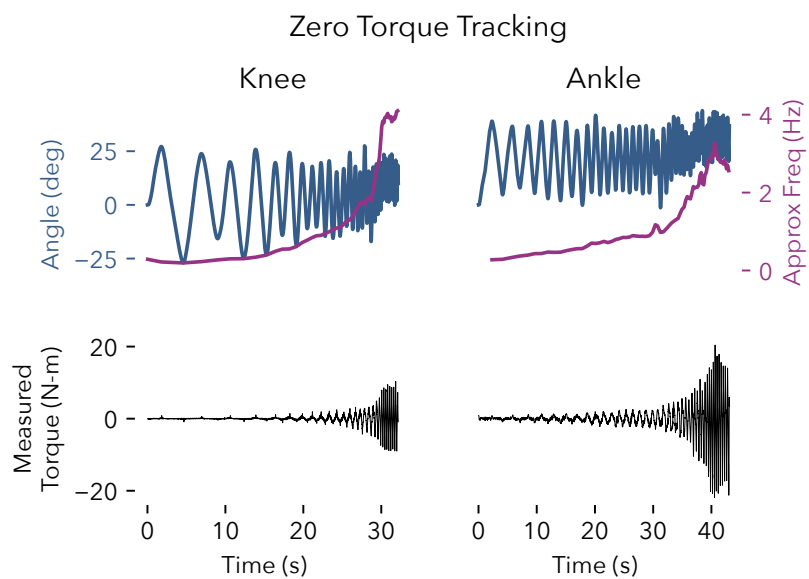


Figure 2.11: Zero torque tracking of knee and ankle joints. The prosthesis was fixed to a rigid mount and commanded to maintain zero net joint torque while the knee and ankle joints were manually oscillated (blue) by hand at increasingly fast rate (purple). The resulting measured torque is shown in the second row of axes in black.

3

*Simultated Comparison of Neuromuscular and Impedance  
Controllers*



4

## *Preference Based Optimization*



# 5

## *Experimental Comparison of Neuromuscular and Impedance Controllers*

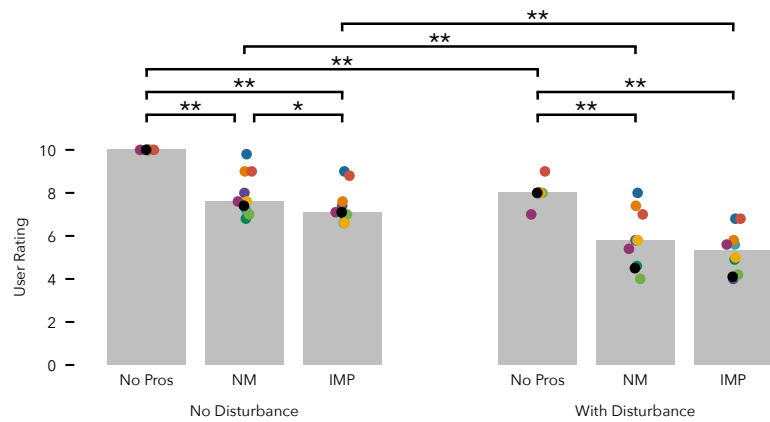


Figure 5.1: Average user ratings accross all trials in both the undisturbed and disturbed walking conditions when walking without the prosthesis (No Pros) and with the Neuromuscular (NM) prosthesis control and impedance (IMP) prosthesis control.

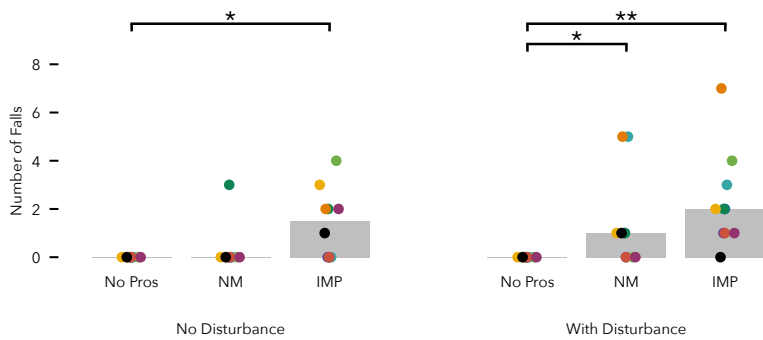


Figure 5.2: Total number of falls accross all trials in both the undisturbed and disturbed walking conditions when walking without the prosthesis (No Pros) and with the Neuromuscular (NM) prosthesis control and impedance (IMP) prosthesis control.

Fall Types	Neuromuscular	Impedance
Fall Forward	1	0
Fall Backwards	6	4
Fall Left	1	0
Fall Right	0	3
Missed Stance / Swing Transition	3	0
Missed Stance 2 / Stance 3 Transition	0	7
Knee Collapse	0	15
Swing Trip	4	12

Table 5.1: Tally of observed reasons for falls accross all subjects and accross both the undisturbed and disturbed walking conditions. Falls were manually classified based on video and logged prosthesis data. An individual Fall can be assigned more than one reason.

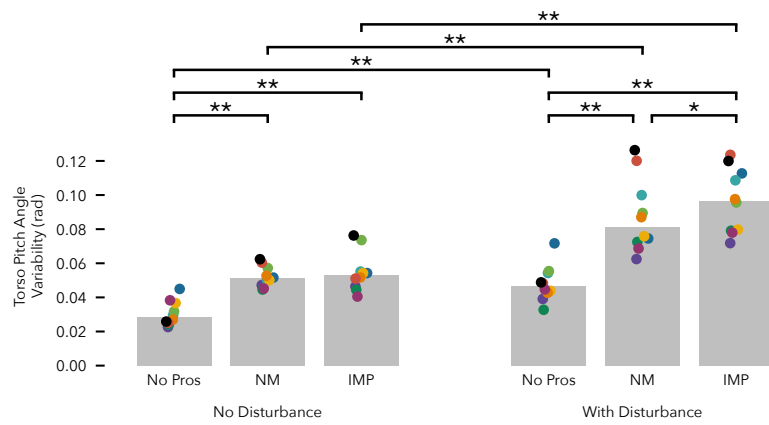


Figure 5.3: Torso pitch angle variation. Angle variation calculated as the inter quartile range of torso angles after the median torso angle trajectory over the strides in a trial is subtracted out. For the prosthesis trials, we report the average variation accross the five trials for each condition. Grey bars show median accross subjects.

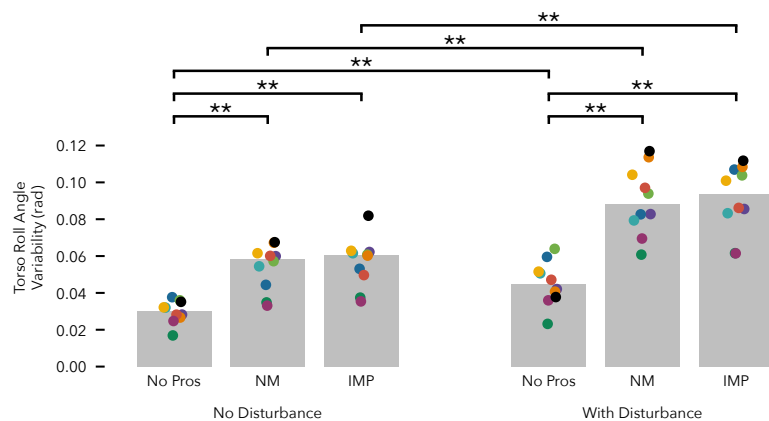


Figure 5.4: Torso roll angle variation. Angle variation calculated as the inter quartile range of torso angles after the median torso angle trajectory over the strides in a trial is subtracted out. For the prosthesis trials, we report the average variation accross the five trials for each condition. Grey bars show median accross subjects.

# 6

## *Swing Control for Avoiding Trips*

### *6.1 Introduction*

Lower limb amputees using state of the art commercial prostheses face a number of gait deficiencies that negatively impact their quality of life (?). Of acute significance among these deficiencies are the increased risk of falling and the related injuries, which can lead to amputees avoiding activity out of a fear falling (?). As falls and their avoidance are linked to swing leg placement in locomotion, active swing control strategies could help to substantially reduce the risk of falling. However, current swing controllers of transfemoral prostheses do little to proactively minimize this risk.

Existing swing phase control approaches for powered prostheses predominantly seek to reproduce the average swing phase behavior of the human leg. Whether the approach is based on trajectory planning (?), impedance control (?), or phase-based control (?), they all treat the swing phase motion as an “open loop” problem with respect to trip hazards, as none of the approaches take the location of the heel and toe of the prosthetic foot with respect to the ground explicitly into account. Therefore, current swing control strategies neglect a clear advantage that robotic prostheses can have over their passive counterparts: the ability to sense and act upon environmental information.

In this work, we develop a swing control strategy to reactively avoid trips with powered transfemoral prostheses that uses visual information about the environment and an estimate of the prosthesis configuration. Some previous studies have explored incorporating visual feedback into the control of leg prostheses. For example, ? developed a state estimator and controller that allowed the ankle joint of a prosthesis to conform to the slope of the ground under the foot. To address the problem of terrain recognition, ? developed a classifier using a LIDAR and an IMU to discriminate between terrains such as flat ground and steps. More recently, ? combined this terrain

classifier with a Bayesian intent classifier (based on (?)) to develop an environment-aware locomotion mode recognition system. In addition, RGBD sensors have been explored as a source of rich environmental information for legged assistance, including gait recognition (?) and stair detection (??). However, none of these previous studies have implemented a control strategy that uses environmental information to reactively govern the motion of a powered prosthesis in real-time.

We present such a real-time reactive control of a powered prosthesis that combines three building blocks. First, we use an extended Kalman filter (EKF) that fuses measurements from an IMU, a LIDAR, and encoders on the prosthesis to estimate the current pose of the prosthetic leg with respect to the ground. Second, we predict likely future leg trajectories with sparse Gaussian process models learned online during swing. Finally, we use the leg pose estimate and trajectory predictions in a fast quadratic-program planner to reactively generate in real time leg joint trajectories that avoid premature toe and heel contact with the ground. To evaluate the proposed control, we compare our method for trip avoidance to a standard non-reactive minimum-jerk trajectory planning approach in a prosthesis walking experiment designed to elicit trips.

## 6.2 Methods

The trip avoidance control we propose involves (1) estimating the position and orientation of the leg (??), (2) predicting the future hip angles and heights (??), and (3) planning corresponding knee and ankle trajectories such that the heel and toe will not contact the ground prematurely (??).

### 6.2.1 Extended Kalman Filter for estimating Leg Position/Orientation

To estimate the position and orientation of the leg, we employ an EKF that fuses information from a LIDAR distance sensor (SICK OD1000), an IMU (YEI Technologies 3-Space sensor), and encoders on the prosthesis (Renishaw Resolute, Netzer DS-25). The EKF filters the nonlinear, discrete-time dynamics given by

$$\begin{aligned} x_t = \begin{bmatrix} q_t \\ p_t \\ \dot{p}_t \end{bmatrix} &= \begin{bmatrix} f_{\text{gyro}}(\omega_t) & 0 & 0 \\ 0 & I_{3 \times 3} & \Delta t I_{3 \times 3} \\ 0 & 0 & I_{3 \times 3} \end{bmatrix} x_{t-1} \\ &+ \begin{bmatrix} 0 \\ \frac{1}{2} \Delta t^2 I_{3 \times 3} \\ \Delta t I_{3 \times 3} \end{bmatrix} \left[ R_{\text{OI}}(q_{t-1}) a_t - \begin{bmatrix} 0 \\ 0 \\ g \end{bmatrix} \right] + w_t \quad (6.1) \\ &= f(x_{t-1}, u_t) + w_t, \end{aligned}$$

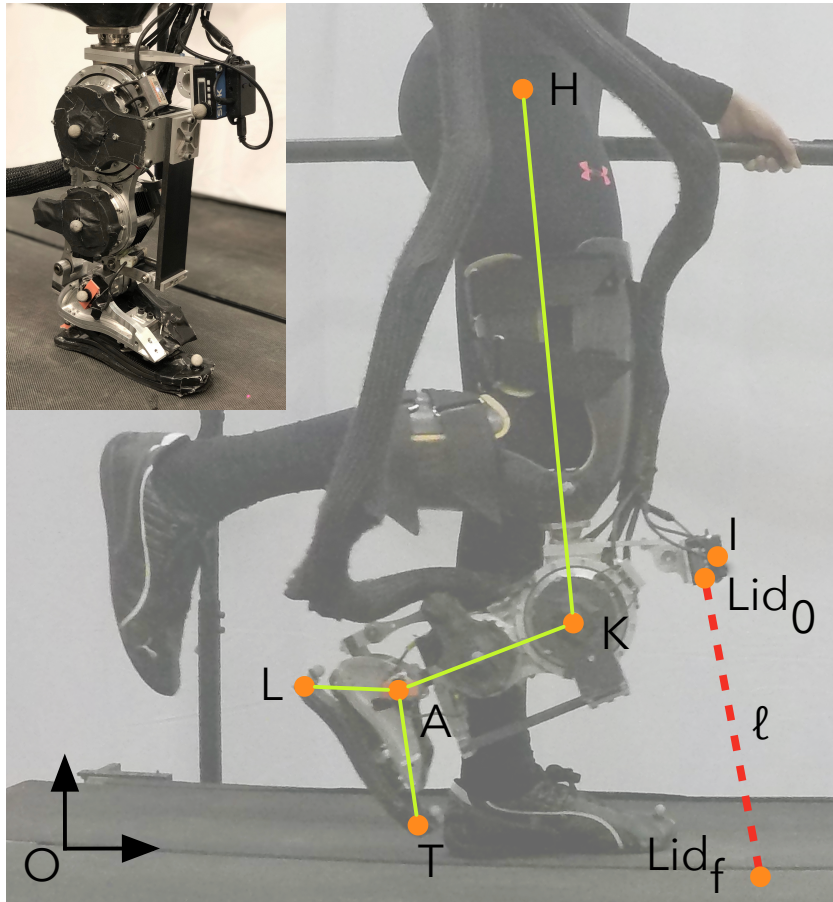


Figure 6.1: Kinematic model of the user and prosthesis used for state estimation and motion planning. The model includes the hip (H), knee (K), ankle (A), heel (L) and toe points (T). Additionally, the start ( $Lid_0$ ) and end ( $Lid_f$ ) points of the LIDAR beam (with length  $\ell$ ) are indicated. The IMU is located at point I. Both the LIDAR and IMU are mounted to the thigh portion of the powered knee-and-ankle prosthesis.

where  $q$  is the quaternion orientation,  $R_{\text{OI}}$  and  $p$  are the rotation matrix and position of the IMU in inertial coordinates,  $\omega$  is the angular rate measured by the gyroscope,  $f_{\text{gyro}}$  integrates the gyroscope rate to update the orientation,  $a$  is the accelerometer measurement,  $u_t = [\omega_t, a_t]^T$ , and  $\Delta t$  is the integration time step (1 ms).

The dynamics are corrupted by process noise  $w_t \sim \mathcal{N}(0, Q_t)$  due to the inaccuracy of the IMU's measurement of the true acceleration and angular velocity. Consequently,  $Q_t$  is given by

$$Q_t = \frac{\partial f}{\partial u} \Big|_{x_{t-1}, u_t} \begin{bmatrix} \sigma_\omega^2 I_{3 \times 3} & 0 \\ 0 & \sigma_a^2 I_{3 \times 3} \end{bmatrix} \frac{\partial f}{\partial u}^T \Big|_{x_{t-1}, u_t}, \quad (6.2)$$

where  $\sigma_\omega^2$  and  $\sigma_a^2$  are the gyroscope and accelerometer measurement variances, respectively.

To estimate the pose given our sensor measurements, we follow a standard EKF procedure (?), reviewed here for completeness. The EKF state estimation process has two steps: First, we *predict* the next state distribution by forward-propagating the mean  $\hat{x}_{t-1|t-1}$  and covariance of the state estimate  $\Sigma_{t-1|t-1}$  using the dynamics given by ??,

$$\hat{x}_{t|t-1} = f(\hat{x}_{t-1|t-1}, u_t) \quad (6.3)$$

$$\Sigma_{t|t-1} = F_t \Sigma_{t-1|t-1} F_t^T + Q_t, \quad (6.4)$$

where  $F_t = \partial f / \partial x|_{\hat{x}_{t-1|t-1}}$ .

Next, we incorporate information from noisy sensor observations to *update* the state estimate. To do this, we utilize a observation model given by  $z_t = h(x_t) + v_t$ , where  $v_t \sim \mathcal{N}(0, R)$ , and the following update equations:

$$K_t = \Sigma_{t|t-1} H_t^T \left( H_t \Sigma_{t|t-1} H_t^T + R \right)^{-1} \quad (6.5)$$

$$\hat{x}_{t|t} = \hat{x}_{t|t-1} + K_t (z_t - h(\hat{x}_{t|t-1})) \quad (6.6)$$

$$\Sigma_{t|t} = (I - K_t H_t) \Sigma_{t|t-1} \quad (6.7)$$

where  $z_t$  are the actual sensor measurements and  $H_t = \partial h / \partial x|_{\hat{x}_{t-1|t}}$ .

The observations in our EKF formulation use the kinematic model shown in ???. We calibrate this model using ground truth data from a VICON motion capture system. In our application we incorporate three observations:

1. The expected acceleration vector points up in the global coordinate frame,

$$h_1(x_t) = \{R_{\text{OI}}(q)\}_{\text{row } 3} \quad (6.8)$$

$$z_1 = a \quad (6.9)$$

2. The expected LIDAR measurement given the position of the IMU,

$$h_2(x_t) = \{\ell : \{p_{\text{OLID}_f}(x_t, \ell)\}_{\text{row}3} = 0\} \quad (6.10)$$

$$z_2 = \ell_{\text{meas}}, \quad (6.11)$$

where  $p_{\text{OLID}_f}$  is the location of the laser beam endpoint represented in the global coordinate system,  $\ell = \|\overrightarrow{\text{LID}_0 \text{LID}_f}\|$  is the modeled laser beam length, and  $\ell_{\text{meas}}$  is the actual measured LIDAR distance.

3. During stance, the toe point coincides with the origin (active 200 m/s after stance begins until toe-off)

$$h_3(x_t) = p_{\text{OT}}(x_t, \theta_k, \theta_a) \quad (6.12)$$

$$z_3 = [0 \ 0 \ 0]^T \quad (6.13)$$

where  $p_{\text{OT}}$  is the location of the toe in the inertial frame, and  $\theta_k$  and  $\theta_a$  are the measured knee and ankle angles.

The measurement noise for these observations is given by

$$R = \begin{bmatrix} \sigma_a^2 I_{3 \times 3} & 0 \\ 0 & \sigma_l^2 \end{bmatrix} \quad (6.14)$$

during swing and

$$R = \begin{bmatrix} \sigma_a^2 I_{3 \times 3} & 0 & 0 \\ 0 & \sigma_\ell^2 & 0 \\ 0 & 0 & \sigma_f^2 I_{3 \times 3} \end{bmatrix} \quad (6.15)$$

during stance. In these equations,  $\sigma_a^2$  is the accelerometer variance,  $\sigma_\ell^2$  is the LIDAR measurement variance, and  $\sigma_f^2$  is the foot position variance.

To further improve the EKF's state estimate, we enforce a number of constraints using the methods provided by ?. Specifically, we enforce three equality constraints:

1. First, we require that the quaternion has unit norm

$$1 = q_1^2 + q_2^2 + q_3^2 + q_4^2. \quad (6.16)$$

2. Second, we prevent the yaw component of the orientation  $q$  from drifting. To do this, we convert the  $q$  to ZYX Euler angles and enforce  $\phi_z = 0$ ,

$$0 = \text{atan2}\left(2(q_1 q_4 + q_2 q_3), 1 - 2(q_3^2 + q_4^2)\right). \quad (6.17)$$

3. Finally, during stance we further constrain the toe's  $x$  and  $y$ -coordinates to 0,

$$\begin{bmatrix} 0 \\ 0 \end{bmatrix} = \{p_{\text{OT}}(x_t, \theta_k, \theta_a)\}_{\text{rows 1 and 2}}. \quad (6.18)$$

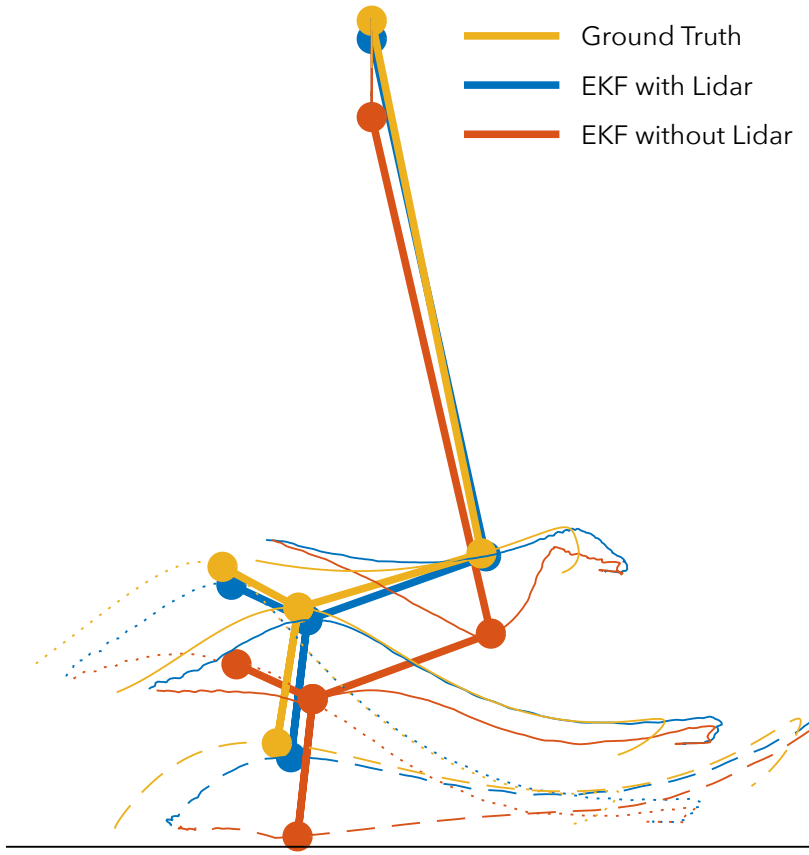


Figure 6.2: Trajectories of extended Kalman Filter (EKF) estimate of the position of the leg during swing (blue). Ground truth positions given by motion capture (yellow). EKF estimate without LIDAR information shown in red. Thick lines show the leg configuration at peak toe height during swing. Dotted lines indicate heel trajectories while dashed lines show the toe trajectories. Knee and ankle trajectories given by solid lines.

In addition, we use inequality constraints to ensure the toe and heel do not penetrate the ground,

$$0 \leq \{p_{OT}(x_t, \theta_k, \theta_a)\}_{\text{row } 3}, \quad (6.19)$$

$$0 \leq \{p_{OL}(x_t, \theta_k, \theta_a)\}_{\text{row } 3}. \quad (6.20)$$

We enforce these constraints by solving the following quadratic program after each update step,

$$\hat{x}_{t|t}^{\text{proj}} = \underset{x}{\operatorname{argmin}} \left( x - \hat{x}_{t|t} \right)^T \Sigma_{t|t}^{-1} \left( x - \hat{x}_{t|t} \right), \quad (6.21)$$

such that

$$A_{\text{eq}}x = b_{\text{eq}}, \quad (6.22)$$

$$A_{\text{ineq}}x = b_{\text{ineq}}, \quad (6.23)$$

where  $A_{\text{eq}}$ ,  $b_{\text{eq}}$ ,  $A_{\text{ineq}}$ , and  $b_{\text{ineq}}$  are derived from linearizing the equality and inequality constraints.

To identify the appropriate parameters of the Kalman filter, we collected ground truth training and testing kinematic data using a Vicon motion capture system and optimized the parameters of the EKF to minimize the error of the kinematic estimate. The parameters we optimized were the rotation of the LIDAR with respect to the hip, the translation between the LIDAR and the IMU, and  $\sigma_\omega$ ,  $\sigma_a$ ,  $\sigma_\ell$ , and  $\sigma_f$ .

?? shows an example of the resulting EKF estimates of the hip, knee, ankle, heel, and toe positions during swing (blue stick figure and traces) compared to the ground truth obtained from the motion capture system (yellow) and an EKF estimate without the LIDAR sensor information integrated (red). Over the entire test data set, the root mean squared error of the estimated heel and toe positions during swing is 18.6 mm for the EKF with LIDAR information. In contrast, the EKF without LIDAR information has an error of 46.7 mm. Thus, including the LIDAR sensor data reduces the error by 60%.

### 6.2.2 Gaussian Process Hip Trajectory Prediction

To predict the future hip angle and height trajectories, we train sparse Gaussian process models using the FITC approximation (?). The sparse approximation ensures the computational complexity at test time is independent of the training data set size, providing consistent real time performance. Throughout the swing phase, the learned hip angle and height distributions are conditioned on the swing trajectories completed so far to predict the distribution of the future trajectories for the rest of the swing (example shown in ??). Our algorithm then uses the means of these conditional distributions in the motion planning phase (compare ??).

For example, to calculate the conditional mean of future hip angles, we first compute the joint distribution of completed ( $\theta_h^c$ ) and future ( $\theta_h^f$ ) hip angles,

$$P(\theta_h^c, \theta_h^f) = \mathcal{N}(\mu_{\text{fitc}}, \Sigma_{\text{fitc}} + K(t_{\text{joint}}, t_{\text{joint}})) \quad (6.24)$$

$$= \mathcal{N}\left(\begin{bmatrix} \mu_c \\ \mu_f \end{bmatrix}, \begin{bmatrix} \Sigma_{c,c} & \Sigma_{c,f} \\ \Sigma_{f,c} & \Sigma_{f,f} \end{bmatrix}\right), \quad (6.25)$$

where  $\mu_{\text{fitc}}$  and  $\Sigma_{\text{fitc}}$  are obtained from equation 11 in (?) and  $K(t_{\text{joint}}, t_{\text{joint}})$  is an additional noise term given by a rational quadratic kernel (?) that correlates the predicted angles across time, which results in smooth predicted trajectories. The mean of the conditional distribution  $P(\theta_h^f | \theta_h^c)$  is then given by

$$\mu_f^{\text{cond}} = \mu_f + \Sigma_{f,c} \Sigma_{c,c}^{-1} (\mu_c - \theta_h^c). \quad (6.26)$$

As the inversion of  $\Sigma_{c,c}$  is the most computationally expensive component of ??, we use at most the last 10 hip angles and heights (sampled at 100 Hz) when calculating the conditional mean (compare ??).

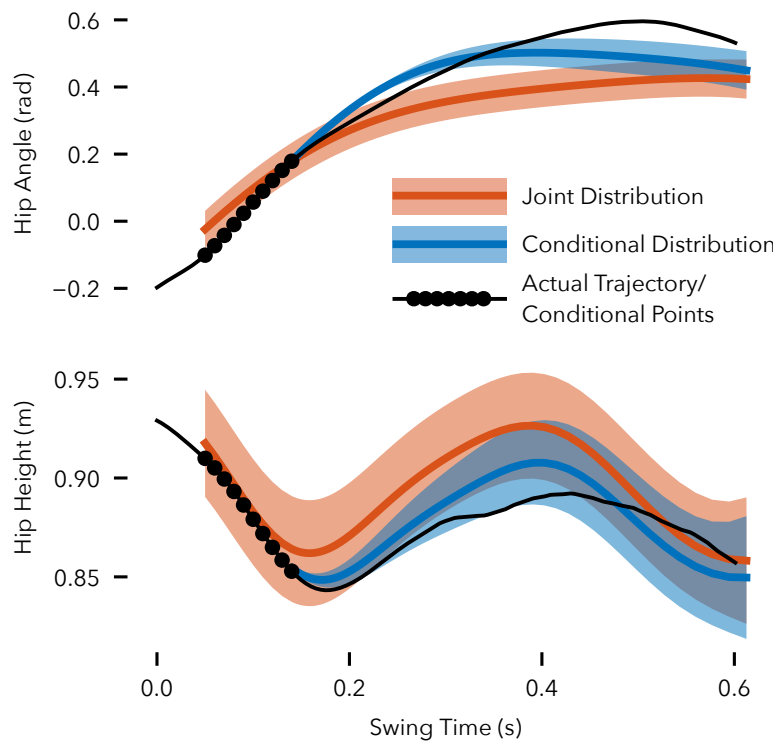


Figure 6.3: Example of hip angle and height trajectory predictions 0.15 s into swing. The prediction algorithm uses the previous 10 measured hip angles and heights (sampled at 100 Hz, black dots) along with the learned joint distributions of hip angles/heights versus time (red) to obtain the conditional distributions of future hip angles/heights (blue). The planning algorithm uses the means of the conditional distributions to generate knee and ankle trajectories. The actual hip height and angle trajectories are shown in black.

### 6.2.3 Trajectory Planning Quadratic Program Formulation

To obtain reactive control of the prosthesis swing leg motion, we plan future swing trajectories with a fast quadratic program (QP) operating at 100 Hz. The QP includes equality constraints, which ensure the trajectories progress smoothly from the current position to the desired end position, and inequality constraints, which avoid premature ground contact of toe and heel of the prosthesis. Because in our formulation the QP can only solve for one joint at a time, we first solve for the ankle trajectory assuming the knee trajectory found in the previous time step, and then use this updated ankle trajectory to solve for the new knee trajectory.

?? provides more details of the actions of the trajectory planner algorithm. For example, at a time of about 150 ms into the swing

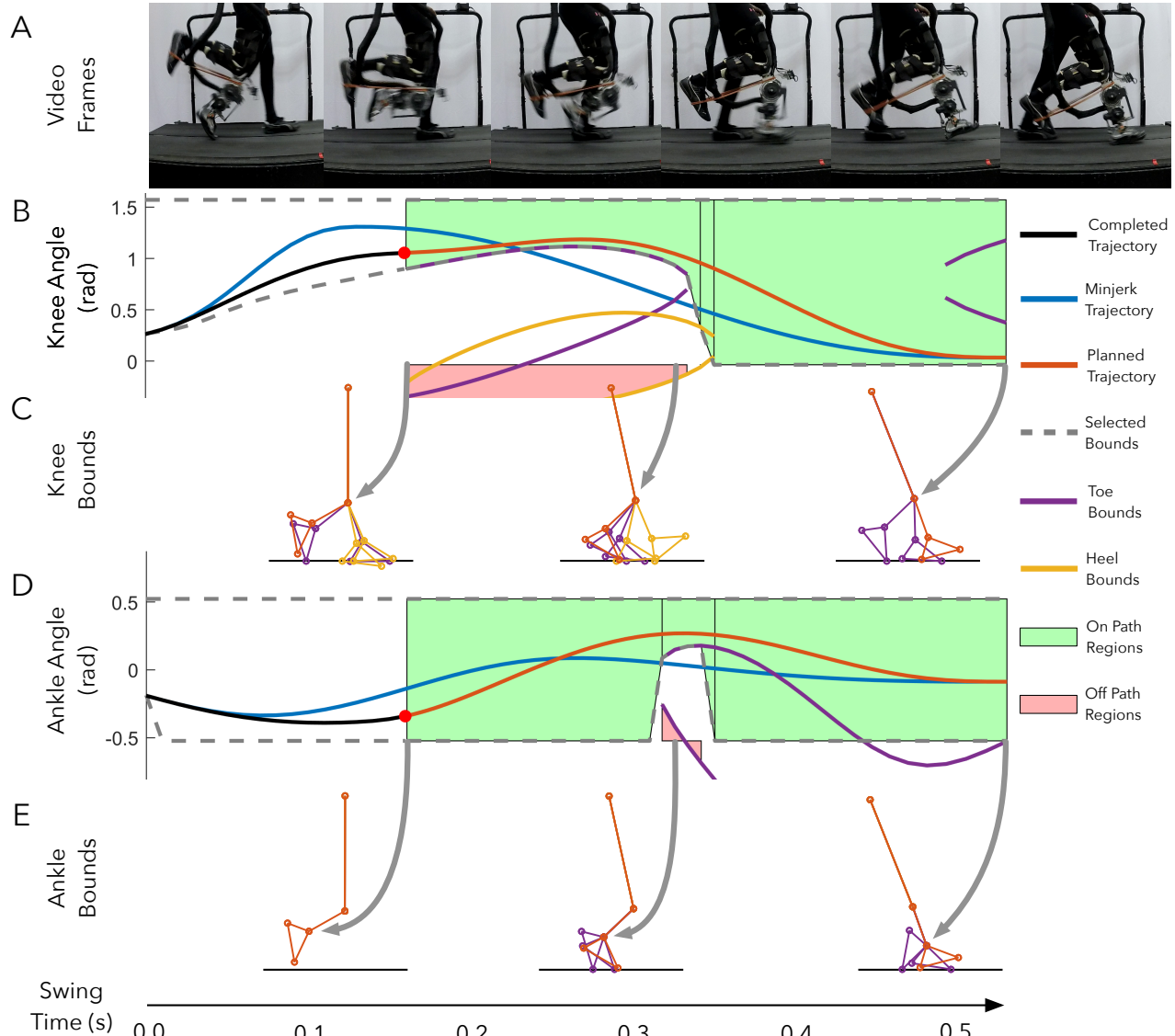


Figure 6.4: Planning Algorithm Steps: Panels B and D show the generated knee and ankle trajectories respectively. The planned trajectory (red) lies within the computed bounds (dashed gray). In contrast, standard minimum jerk trajectories (blue) do not respect the bounds, thereby increasing the tripping hazard. Panels C and E show examples of inverse kinematics (IK) solutions for toe (purple) and heel

phase, the algorithm solves

$$\theta_k^{\text{toe bnd}} = \left\{ \theta_k : \{p_{\text{OT}}(\theta_h, z_h, \theta_k, \theta_a)\}_{\text{row 3}} = 0 \right\} \quad (6.27)$$

$$\theta_k^{\text{heel bnd}} = \left\{ \theta_k : \{p_{\text{OL}}(\theta_h, z_h, \theta_k, \theta_a)\}_{\text{row 3}} = 0 \right\} \quad (6.28)$$

at a set of sample times spanning the remaining swing trajectory to obtain a planned knee trajectory (red trace in ??B). Figures ??C and E show the predicted inverse kinematics (IK) solutions at characteristic points into the swing for the knee and ankle respectively, with solutions leading to toe contact shown in purple and solutions leading to heel contact shown in yellow. For each contact point, there are typically two solutions, one lower bound, for which the joint angle cannot cross from above, and one upper bound, for which the joint angle cannot cross from below.

Often, the valid leg configurations span disjointed regions in the configuration space (green and red regions in ??B and D). Therefore, the planner next identifies a valid sequence of regions for the trajectory to traverse in a four step procedure. First, the planner identifies critical points along the predicted trajectory at which any bound activates or deactivates. Second, at each critical point, the planner sorts the bound angles from largest to smallest and iterates through them to define regions between successive upper and lower bounds. Third, the planner defines a graph over the regions with edge weights equal to the average squared angle minus the volume of the child region. This cost favors a sequence of regions that are large and thus safe to travel through and avoids regions that require excessive joint flexion or extension. Dijkstra's algorithm is then used to find a valid sequence of regions that minimizes this cost (?). Finally, so that the generated trajectories do not get too close to the identified bounds, a buffer is added to the bounds. This buffer takes the form

$$\theta_{\text{buf}} = \theta_{\text{buf}}^0 \sin \left( \pi \frac{t - t_0}{t_f - t_0} \right), \quad (6.29)$$

where  $\theta_{\text{buf}}^0$  is either  $5^\circ$  or  $-5^\circ$  for lower and upper bounds respectively,  $t$  is the future swing time, and  $t_0$  and  $t_f$  are the current and final swing times.

After identifying the bounded regions, the planner generates the trajectory for a specific joint by solving a quadratic program. The trajectory of each joint is represented by three, fifth-order polynomial

splines,

$$\theta_1(t) = a_{01} + a_{11}t + \dots + a_{51}t^5 = [1 \ t \ \dots \ t^5]a_1 \quad (6.30)$$

$$T_0 \leq t < T_1 \quad (6.31)$$

⋮

$$\theta_3(t) = a_{03} + a_{13}t + \dots + a_{53}t^5 = [1 \ t \ \dots \ t^5]a_3 \quad (6.32)$$

$$T_2 \leq t < T_F, \quad (6.33)$$

and solved for by the following QP,

$$a^* = \operatorname{argmin}_a \frac{1}{2}a^T(H_\theta + wH_{\ddot{\theta}})a, \quad (6.34)$$

where  $a = [a_1^T \ a_2^T \ a_3^T]^T$ ,  $H_\theta$  and  $H_{\ddot{\theta}}$  encode quadratic costs on angle and jerk respectively, and  $w$  is a weight parameter. The solution is subject to the inequality constraints

$$\theta(t) \leq \theta_{\max}(t), \quad \forall t \quad (6.35)$$

$$\theta(t) \geq \theta_{\min}(t), \quad \forall t \quad (6.36)$$

$$\dot{\theta}(t) \leq \dot{\theta}_{\max}, \quad \forall t \quad (6.37)$$

$$\dot{\theta}(t) \geq \dot{\theta}_{\min}, \quad \forall t, \quad (6.38)$$

which ensure the trajectory lies within the identified bounds and respects velocity limits, and to the equality constraints

$$\theta(T_0) = \theta_0 \quad (6.39)$$

$$\dot{\theta}(T_0) = \dot{\theta}_0 \quad (6.40)$$

$$\ddot{\theta}(T_0) = \ddot{\theta}_0 \quad (6.41)$$

$$\theta(T_F) = \theta_F \quad (6.42)$$

$$\dot{\theta}(T_F) = 0 \quad (6.43)$$

$$\ddot{\theta}(T_F) = 0 \quad (6.44)$$

$$\theta_1(T_1) = \theta_2(T_1) \quad (6.45)$$

$$\dot{\theta}_1(T_1) = \dot{\theta}_2(T_1) \quad (6.46)$$

$$\ddot{\theta}_1(T_1) = \ddot{\theta}_2(T_1) \quad (6.47)$$

⋮

which ensure the trajectory starts at the current and terminates at the desired positions, velocities, and accelerations and that the splines join together smoothly. If the QP fails to find a trajectory that can satisfy the constraints, the last found valid trajectory is reused for the next time step. In addition, at the first iteration, the ankle trajectory planner uses the output of the minimum jerk trajectory planner to solve the inverse kinematics for the bounds.

#### 6.2.4 Experimental Procedure

We tested the ability of the proposed trip avoidance control to reduce the incidence and severity of trips while walking with the powered transfemoral prosthesis shown in ?? (previously described in citation omitted.) To evaluate the performance of the system, an able-bodied user walked with the prosthesis while attempting to elicit trips by lowering the hip in swing. During the stance phase, the prosthesis randomly decided to either use the proposed swing control or to use standard minimum jerk trajectories that do not consider the tripping hazard. The user was not aware of which controller would be used in the upcoming swing. The user completed a total of ten one minute walking trials.

We examined several outcomes for evaluating the control performance. First, we examined the distribution of knee angles at the beginning of stance. Large knee angles at the beginning of stance indicate premature landing due to toe-strike instead of heel strike. Ideally, the landing angle is close to the desired final angle of 2 degrees. Second, we checked the integral of the ground reaction force during swing. If this quantity is large, it indicates scuffing of the toe on the ground. Finally, we examined the relationship between the hip and toe heights during swing. If our controller is working as intended, the toe height during swing should have a decreased sensitivity to the hip height.

### 6.3 Results

?? shows the knee and ankle swing trajectories generated by the proposed control (blue) and by a standard jerk minimization control (red) during normal walking and trip elicitation. During undisturbed walking, the trajectories produced by both control strategies are similar. However, the proposed control strategy has a tendency to keep the knee flexed for longer and then extends it faster towards the end of swing. In addition, in a few steps, the proposed controller flexed the ankle significantly more than did the standard minimum jerk control. These trends are exaggerated during trip elicitation. There are more knee trajectories in which the knee stays flexed for longer, thereby creating more ground clearance. In addition, the ankle flexes earlier, which will help to create more foot clearance when the hip is suddenly lowered in early swing.

We used video and audio recordings of the trials, as well as data from the prosthesis, to manually classify trips as those swing trajectories that end with toe strike or during which the foot scuffed on the ground. We find that over the ten minutes of walking, the mini-

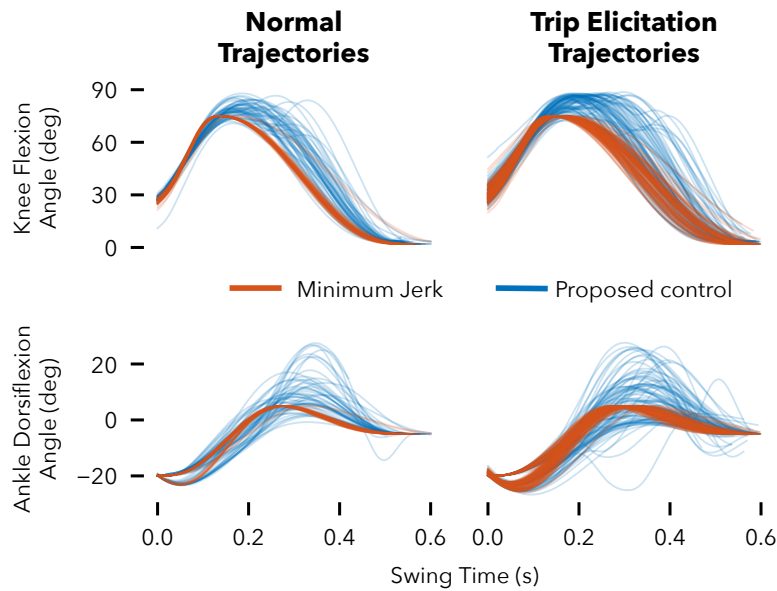


Figure 6.5: Knee and ankle trajectories produced during normal walking and while eliciting trips. To avoid tripping during trip elicitation trials, trajectories generated by the proposed approach often flex the knee to a greater degree and for longer before quickly extending at the end of swing. At the ankle joint we see overall greater variability in the generated trajectories during the trip elicitation condition versus normal walking.

minimum jerk control produced 109 trips while the proposed approach produced 35 trips, reducing the trip rate by 68%.

To further examine the performance of the two control strategies, we used kernel density estimates of the landing knee flexion angle, a measure of the propensity for tripping, and integrated ground reaction force (GRF) during swing, a measure of the propensity for foot scuffing. ?? shows the distributions of the landing angle of the prosthesis at the end of swing for the proposed swing control (blue) and for the standard minimum jerk swing control (red) during the trip elicitation condition. We observe the minimum jerk control is much more likely to generate a swing trajectory that ends prematurely with a large knee flexion angle, which is indicative of toe contact instead of heel contact at the end of swing. The distributions of the integrated GRFs suggests the minimum jerk control produced a larger percentage of swings with high ground reaction forces than the proposed control, indicating an increased frequency and severity of toe scuffing during swing (??).

We can also ask the question, “For steps during which the prosthesis used trajectories generated by the proposed control, would the user have tripped had the prosthesis used a minimum jerk trajectory?” To answer this question, we can use the kinematics model shown in ?? along with ground truth hip height and hip angle data captured via a motion capture system, to estimate the location of the toe had the knee and ankle perfectly followed the desired trajec-

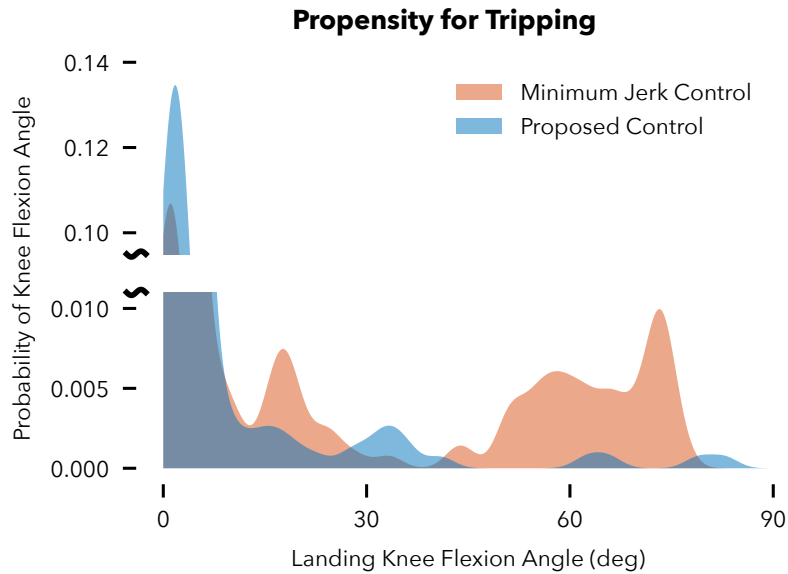


Figure 6.6: Kernel density estimate of the probability of various landing knee flexion angles with the proposed swing control (blue) and standard min-jerk swing control (red). Large landing knee angles indicate premature toe contact during swing.

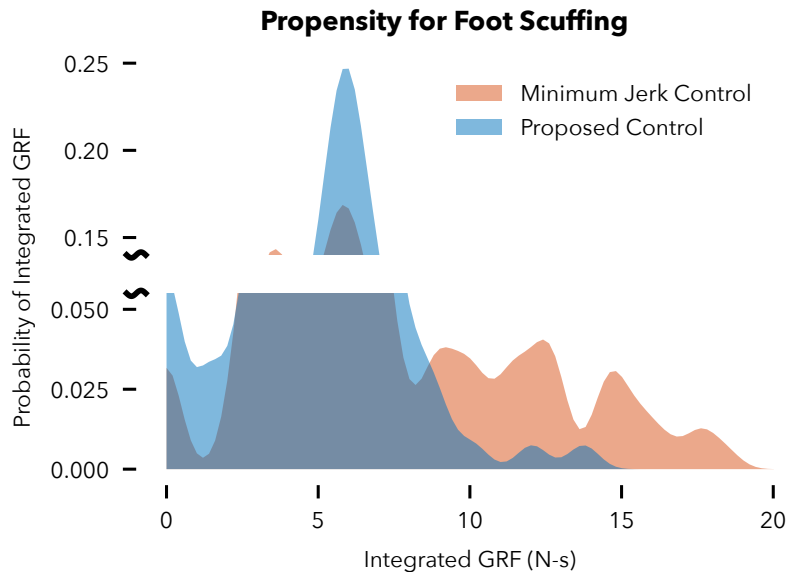


Figure 6.7: Kernel density estimate of the probability of various integrated ground reaction force values for the proposed swing control (blue) and standard min-jerk swing control (red). Large integrated GRF during the swing phase is indicative of the toe scuffing on the ground.

ries produced by each control scheme. This analysis predicts that the prosthesis would have tripped or scuffed the toe on the ground during 22% of the steps if we had used the minimum jerk trajectory. In contrast, it predicts a trip or scuff rate of 5% had we perfectly followed the trajectories generated by the proposed control.

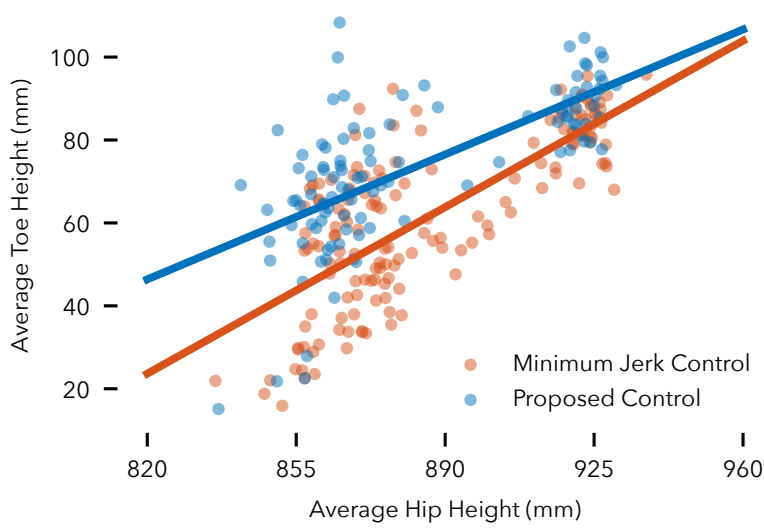


Figure 6.8: Average toe height vs average hip height for the proposed swing control (blue) and standard min-jerk swing control (red). The toe height during swing is less sensitive to the hip height when using the proposed swing control than when using the min-jerk swing control.

Finally, ?? shows the relationship between the average toe and hip heights during swing for both control schemes. The toe height of the prosthesis when controlled by the proposed control is less sensitive to decreases in the hip height than it is when using the standard minimum jerk control.

#### 6.4 Discussion

We presented initial work toward a real-time reactive control of powered prostheses to help amputees avoid tripping in the swing phase of gait. At any time during swing, the proposed control uses a laser range finder and an inertial measurement unit to estimate the current pose of the prosthesis, predicts the future hip angle and height based on trained Gaussian process models, and then plans new knee and ankle joint trajectories that ensure neither the toe nor heel contacts the ground prematurely. Our results indicate the proposed control approach can substantially reduce the incidence of trips and reduce the severity and frequency of toe scuffing.

To the best of our knowledge, this work is the first demonstration of lower limb prosthetic control that integrates perception feedback

in real-time and that proactively ameliorates the falling hazard amputees face. Previous research in this area has largely focused on detecting stumbles *after* they have occurred. For example, ? and ? have proposed classifiers that can detect trips during swing and predict whether a lower or raising strategy should be used in response. Similarly, ? have proposed a method that can detect stumbles and classify them as trips during swing or slips during stance. However, these previous studies have not proposed concrete control actions to preempt stumbles or to properly react in the event that a stumble is detected. Our results motivate further research into such proactive and reactive approaches, closing the perception-action loop for improving gait robustness with robotic prostheses.

Several avenues for future work exist. First, in our current study only one able-bodied user tested the proposed control. Further experiments with amputee subjects are needed to verify the system provides benefits to this population. For instance, amputees accustomed to walking with passive prostheses show significantly altered hip kinematics (?), which could affect the control behavior. However, the proposed control should be able to properly adapt to these behavior differences, as the Gaussian process models are trained for specific users. Second, although trips during swing are one of the most common failure modes we encounter with our powered prostheses, these events are still rare and many hours of normal walking are required to observe a sufficient number of trips and compare controllers. As a result, we actively induced trips by sudden drops in hip height during swing, which does not exactly reflect the situations in which trips occur. Specifically, trips can happen due to subtle changes in leg kinematics, and it remains to be seen in experiments if our approach can avoid trips in these more subtle situations.

At the implementation level, there is also room for further exploration. To keep the computational costs low, we used quadratic programs that iterate between finding solutions for the ankle and knee joints. While this iterative approach is fast when compared to trajectory optimization methods that deal with multiple joints simultaneously, the iterations occasionally get stuck when the planner for one joint trajectory cannot find a solution based on the assumed fixed trajectory of the other joint. Moreover, if a solution cannot be found, the current approach simply reuses the last identified trajectory, rather than moving the trajectory to be more safe, even if it cannot fully satisfy the bounds. It seems worthwhile to investigate whether non-convex trajectory optimization methods such as CHOMP (?), in which the bounds are represented as soft rather than hard constraints, can help solve for the knee and ankle trajectories simultaneously without sacrificing computational speed.

In addition, several technical simplifications can be considered to bring this technology closer to commercialization. We used an accurate and expensive laser distance sensor, eyeing future research in obstacle scanning and avoidance capabilities. However, for simple ground plane avoidance, inexpensive infrared distance sensors such as those used by ? are likely sufficient. It may also be possible to simplify the trajectory planning phase by, for example, forgoing formal guarantees on satisfying bounds and instead relying on heuristics to increase knee and ankle flexion and adjust timing in response to decreased hip height during swing.

Our immediate goal, however, is to generalize the presented approach to incorporating perception in control beyond the avoidance of flat ground. We are currently investigating the approach's ability to plan trajectories around obstacles that are scanned by the laser range finder. Previous studies such as ? with able-bodied subjects have shown that vision plays a crucial role in both planning and control of the lower limb motion over obstacles. We also envision using the approach to target objects instead of avoiding them. For example, a prosthetic leg could scan, recognize, and target secure foot holds and stair treads, or provide enhanced sports capabilities by targeting and kicking a ball.



# 7

## *Robust and Adaptive Stance Control via Extended Kalman Filter-based Phase Estimation*

### *7.1 Introduction*

The number of lower limb amputees in the United States is projected to increase from 1.6 million in 2005 to 3.6 million in 2050 (?). Expected causes include increases in the rates of vascular disease, diabetes, and the size of the elderly population. Prosthetic legs currently prescribed to these lower limb amputees are mostly passive or semi-passive devices; unlike human limbs, they cannot produce positive net work over a gait cycle. Consequently, amputees often suffer from slow walking speeds, high energy consumption (?), and an increased risk of falling (?). Development of active powered prostheses may help address these gait deficiencies and improve the quality of life for amputees.

A variety of strategies have been proposed to control active-powered prostheses. Currently, the most widely used control method for powered transfemoral prostheses is finite state impedance control. This strategy divides the gait cycle into several discrete phases, each with a different function mapping from joint angle and speed to torque (?). This control method relies on the detection of gait events, such as joint angles crossing thresholds, to trigger phase transitions that may cause abrupt changes in torque output as well as unreliable responses to gait disturbances.

To achieve a more smooth and robust control of lower limb prostheses, researchers have investigated alternative approaches. One such alternative uses models of the human neuromuscular system. In this approach, the phase of gait is implicitly captured in the muscle states that emerge from the interplay between multi-segment limb dynamics, muscle dynamics, and reflexes (??). A downside to these approaches, however, is that they often involve many parameters that may be difficult to tune, thus limiting clinical applicability. Another

alternative approach is exemplified with the phase variable controller proposed by ?. This controller explicitly derives a continuous phase estimate by comparing the hip angle to its integral. This approach may be sensitive to step-to-step changes in gait due to drift in the hip angle integral term. In later work, ? eliminated the reliance on the hip integral by re-introducing discrete state transitions based on thigh angle and velocity thresholds. However, this approach could face similar robustness issues as the previously described finite-state impedance control.

Here we propose a control strategy for lower limb prostheses that is built on a robust and smooth estimate of the phase of gait and does not require a large number of tuning parameters. In ??, we present an Extended Kalman Filter (EKF) that estimates the phase and its rate of change during the stance portion of gait based on a multitude of sensor measurements. We then use sparse Gaussian Process (GP) observation models to learn relationships between phase and sensor measurements for specific users and to choose the appropriate control actions for the prosthesis. In ??, we evaluate the performance of the proposed controller with experiments on able-bodied subjects and a single amputee subject. Finally, in ?? we discuss the results and highlight potential limitations of this study as well as avenues for future research.

## 7.2 *Methods*

The proposed prosthesis controller consists of two components. The first is an Extended Kalman Filter (EKF) that estimates the gait phase, defined as the percent of stance completed so far (??). Ideally, the phase estimate starts at zero at heel strike and reaches one precisely at toe-off. The second component is a set of control surfaces, which are functions of phase and phase velocity, that provide desired knee and ankle angles, velocities, and feed forward torques for generating the prosthesis stance behavior (??).

### 7.2.1 *GP-EKF for estimating phase*

In contrast to the previously described phase variable approach for phase estimation in prostheses (?), which uses a single source of information, we take a sensor-fusion approach and combine angle and velocity information from the hip, knee, and ankle joints of the prosthetic limb. An IMU mounted to the thigh portion of CMU's powered knee-and-ankle prosthesis provides information about the user's hip motion, and encoders on the prosthesis provide information about the knee and ankle joints. We use these observations in

an Extended Kalman filter (EKF) to estimate the phase and phase velocity during stance. The EKF assumes the linear, discrete time phase dynamics

$$\begin{aligned} x_t &= \begin{bmatrix} \phi_t \\ \dot{\phi}_t \end{bmatrix} = \begin{bmatrix} 1 & \Delta t \\ 0 & 1 \end{bmatrix} \begin{bmatrix} \phi_{t-1} \\ \dot{\phi}_{t-1} \end{bmatrix} + w_t \\ &= Ax_{t-1}, \end{aligned} \quad (7.1)$$

where  $\phi$  is the phase,  $\dot{\phi}$  is the rate of change of phase,  $\Delta t$  is the integration time step and  $w_t \sim \mathcal{N}(0, Q)$ . We set

$$Q = \begin{bmatrix} 0 & 0 \\ 0 & \sigma_{\dot{\phi}}^2 \end{bmatrix}, \quad (7.2)$$

with  $\sigma_{\dot{\phi}}^2 = 1e-7$ . These dynamics encode the assumption that phase should evolve continuously, at a roughly constant rate.

Observations of the prosthesis-side hip, knee, and ankle angles and velocities inform the evolution of the above dynamics. For the joint angles, the observation models are of the form

$$z_t^{\theta_j} = h^{\theta_j}(x_t) + v_t^{\theta_j} = \text{GP}_{\mu}^{\theta_j}(\phi_t) + v_t^{\theta_j}, \quad (7.3)$$

where  $\text{GP}_{\mu}^{\theta_j}$  is the mean of a learned Gaussian Process (GP) model of the angle of joint  $j$  as a function of the phase  $\phi$  and  $v_t^{\theta_j} \sim \mathcal{N}(0, \text{GP}_{\sigma^2}^{\theta_j}(\phi_t))$ .

Here,  $\text{GP}_{\sigma^2}^{\theta_j}$  is the variance of the same learned GP model.

Similarly, for the joint velocities we use an observation model of the form

$$\begin{aligned} z_t^{d\theta_j/d\phi} &= h^{d\theta_j/d\phi}(x_t) + v_t^{d\theta_j/d\phi} \dot{\phi}_t \\ &= \left( \text{GP}_{\mu}^{d\theta_j/d\phi}(\phi_t) + v_t^{d\theta_j/d\phi} \right) \dot{\phi}_t \end{aligned} \quad (7.4)$$

where  $\text{GP}_{\mu}^{d\theta_j/d\phi}$  is the mean of a Gaussian Process model of the velocity of joint  $j$  (in units of  $d\theta_j/d\phi$ ) as a function of  $\phi$ . In addition,  $v_t^{d\theta_j/d\phi} \sim \mathcal{N}(0, \text{GP}_{\sigma^2}^{d\theta_j/d\phi}(\phi_t))$ , where  $\text{GP}_{\sigma^2}^{d\theta_j/d\phi}$  is the variance of the same learned GP model for joint velocity.

To train the GP observation models, the algorithm maintains a training data set of stance gait data. The training data set includes the joint angles and velocities (in units of  $d\theta_j/d\phi$ ) sampled at 100 Hz as well as the actual corresponding phases and phase velocities during stance. We assume that, in hindsight, the actual phase increased linearly from zero at heel strike to one at toe off and that the actual phase velocity was constant during stance and equal to  $1/T_n$ , where  $T_n$  is the duration of the completed stance phase. We retrain the GP models using this gait data after every five completed steps. To ensure that the test-time performance of the Gaussian Process models

does not degrade as more training data accumulates, we employ the fully independent training conditional (FITC) approximation of the GP (?). This approximation represents the GP using a fixed-size active set of training points. (We use 25 points in our approximation).

With the learned GP observation models, we follow the GP-EKF procedure proposed by ? to obtain an estimate of phase and phase velocity. In this procedure, we first *predict* the next state distribution by propagating the mean  $\hat{x}_{t-1|t-1}$  and covariance  $\Sigma_{t-1|t-1}$  of the state using the dynamics model provided by ??,

$$\hat{x}_{t|t-1} = A\hat{x}_{t-1|t-1} \quad (7.5)$$

$$\Sigma_{t|t-1} = A\Sigma_{t-1|t-1}A^T + Q. \quad (7.6)$$

Next, we *update* the state distribution estimate given measurements  $z_t$  of the joint angles and velocities using the following equations and the GP observation models  $h_t(x_t)$ .

$$K_t = \Sigma_{t|t-1}H_t^T \left( H_t\Sigma_{t|t-1}H_t^T + M_tRM_t^T \right)^{-1} \quad (7.7)$$

$$\hat{x}_{t|t} = \hat{x}_{t|t-1} + K_t \left( z_t - h(\hat{x}_{t|t-1}) \right) \quad (7.8)$$

$$\Sigma_{t|t} = (I - K_t H_t) \Sigma_{t|t-1} \quad (7.9)$$

where,

$$h(x_t) = \begin{bmatrix} \text{GP}_\mu^{\theta_h}(\phi_t) \\ \text{GP}_\mu^{\theta_k}(\phi_t) \\ \text{GP}_\mu^{\theta_a}(\phi_t) \\ \text{GP}_\mu^{d\theta_h/d\phi}(\phi_t)\dot{\phi}_t \\ \text{GP}_\mu^{d\theta_k/d\phi}(\phi_t)\dot{\phi}_t \\ \text{GP}_\mu^{d\theta_a/d\phi}(\phi_t)\dot{\phi}_t \end{bmatrix} \quad (7.10)$$

$$H_t = \frac{\partial h}{\partial x} \Big|_{\hat{x}_{t|t-1}} = \begin{bmatrix} \frac{\partial \text{GP}_\mu^{\theta_h}}{\partial \phi_t} \Big|_{\phi_t} & 0 \\ \frac{\partial \text{GP}_\mu^{\theta_k}}{\partial \phi_t} \Big|_{\phi_t} & 0 \\ \frac{\partial \text{GP}_\mu^{\theta_a}}{\partial \phi_t} \Big|_{\phi_t} & 0 \\ \frac{\partial \text{GP}_\mu^{d\theta_h/d\phi}}{\partial \phi_t} \Big|_{\phi_t} & \text{GP}_\mu^{d\theta_h/d\phi} \\ \frac{\partial \text{GP}_\mu^{d\theta_k/d\phi}}{\partial \phi_t} \Big|_{\phi_t} & \text{GP}_\mu^{d\theta_k/d\phi} \\ \frac{\partial \text{GP}_\mu^{d\theta_a/d\phi}}{\partial \phi_t} \Big|_{\phi_t} & \text{GP}_\mu^{d\theta_a/d\phi} \end{bmatrix} \quad (7.11)$$

$$M_t = \frac{\partial h}{\partial v_t} \Big|_{\hat{x}_{t|t-1}} = \begin{bmatrix} I_{3 \times 3} & 0 \\ 0 & \dot{\phi}_t I_{3 \times 3} \end{bmatrix} \quad (7.12)$$

$$R_t = \text{blkdiag} \left( \text{GP}_{\sigma^2}^{\theta_h}(\phi_t), \text{GP}_{\sigma^2}^{\theta_k}(\phi_t), \text{GP}_{\sigma^2}^{\theta_a}(\phi_t), \text{GP}_{\sigma^2}^{d\theta_h/d\phi}(\phi_t), \text{GP}_{\sigma^2}^{d\theta_k/d\phi}(\phi_t), \text{GP}_{\sigma^2}^{d\theta_a/d\phi}(\phi_t) \right) \quad (7.13)$$

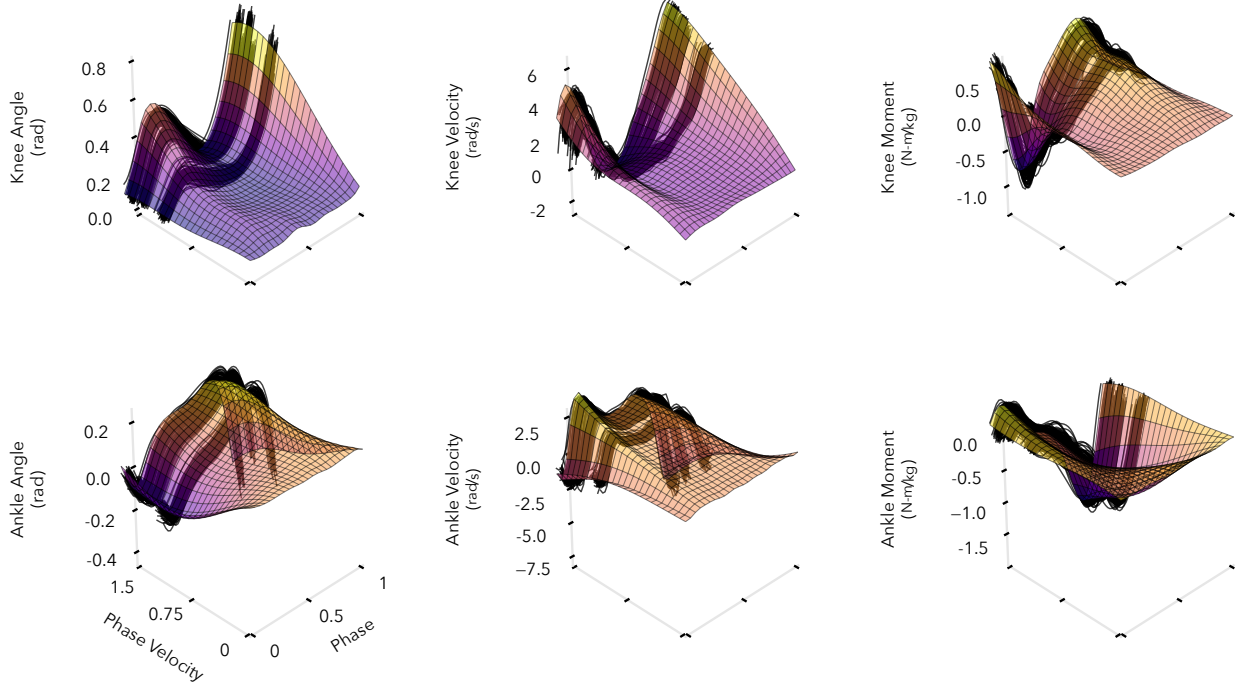


Figure 7.1: Examples of learned control surfaces. We fit the surfaces to gait data from ?. This data includes information for three speeds, 0.8, 1.2, and 1.6 m/s, which are shown as the clustered trajectories in the above panels. For an automatic transition to standing, the surfaces are additionally fit to virtual data that causes the joint angles to approach 5 deg, the velocities to approach 0 deg/s, and the joint torques to approach 0 N-m as the phase velocity goes to zero.

Due to the linearity of Gaussian processes and differentiation, we can analytically obtain derivatives required by ?? using the methods provided by ?.

Finally, we reset the state distribution at heel strike to

$$\hat{x}_0 = \begin{bmatrix} 0 \\ 1/T_{n-1} \end{bmatrix}, \quad \Sigma_0 = 0_{2 \times 2}, \quad (7.14)$$

where  $T_{n-1}$  is the duration of the previous stance.

### 7.2.2 Control Surfaces

We use the mean estimates of the phase  $\phi$  and phase velocity  $\dot{\phi}$  as the inputs into learned control surfaces that provide the desired knee and ankle angles, velocities, and feed-forward torques (Fig. ??). The final desired torques applied to the prosthesis are then given by

$$\tau_d = k_p (\theta_d(\phi, \dot{\phi}) - \theta) + k_d (\dot{\theta}_d(\phi, \dot{\phi}) - \dot{\theta}) + \tau_{ff}(\phi, \dot{\phi}), \quad (7.15)$$

where  $\theta_d$ ,  $\dot{\theta}_d$ , and  $\tau_{ff}$  are the learned control surfaces as functions of the estimated phase and phase velocity,  $k_p$  and  $k_d$  are proportional and derivative gains, and  $\theta$  and  $\dot{\theta}$  are the actual joint angle and velocity.

We learned the control surfaces  $\theta_d$ ,  $\dot{\theta}_d$  and  $\tau_{ff}$ , by regressing the gait data provided by ? for several subjects walking at three speeds, 0.8, 1.2, and 1.6 m/s. We were able to learn the control surfaces using the data from nine subjects. For each subject, we split the gait data into individual stance phases and extracted the knee and ankle angles, velocities, and joint torques. We also assumed that during each stance, the actual phase increased linearly from zero at heel strike to one at toe off and the phase velocity during stance was constant and equal to  $1/T$ , where  $T$  is the duration of stance. We again used sparse GP regression with the FITC approximation to regress the knee and ankle angles, velocities, and torques versus the phase and phase velocity. In this case, we used 100 active vectors to approximate each GP.

The gait data spans the whole range of phases ([0, 1]) but not the whole range of physiological phase velocities, as the gait speed only varies between 0.8 and 1.6 m/s. To ensure the control surfaces generate smooth behaviors at slower speeds and when standing still ( $\dot{\phi} = 0$ ), we additionally trained the GPs on a grid spanning  $\phi \in [0, 1]$  and  $\dot{\phi} \in [0, \min(\dot{\phi}_{\text{data set}})]$  with *virtual* training values derived from interpolating between the average trajectory at 0.8 m/s and desired values at  $\dot{\phi} = 0$ . When  $\dot{\phi} = 0$ , the desired joint angles, velocities and torques were set to 5 deg, 0 deg/s, and 0 N-m, respectively, thereby creating a smooth transition to a standing mode. ?? shows examples of the resulting control surfaces derived from one subject's data.

### 7.2.3 Experimental Protocol

We evaluated the naturalness of gait and the robustness of our proposed controller in experiments conducted with seven able-bodied subjects, and an amputee subject. We additionally present data from an experienced user of the prosthesis (first author of paper), whose gait characteristics induced a different response from the prosthesis. All subjects provided informed consent to IRB-approved protocols. The amputee subject wore the powered prosthesis prototype shown in ??, while able-bodied subjects used a shortened version of the prosthesis attached via an L-shaped adapter. (for more information on prosthesis specifications see (?)). All subjects had at least six hours of prior practice walking on the prosthesis. The able-bodied subjects walked without assistance from handrails, while the amputee subject used the handrails for balance.

We compared our proposed control method to a stance control based on a neuromuscular model of human neurophysiology (?) and to finite state impedance control (?). For these controllers, we generated parameter sets by fitting control parameters to the same nine

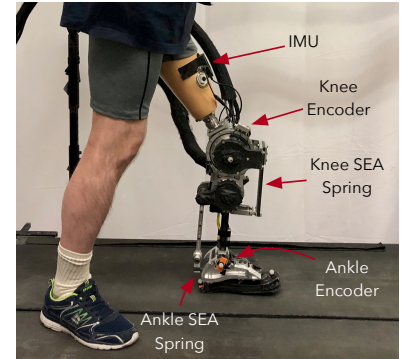


Figure 7.2: CMU powered prosthesis used in experiments. The prosthesis has brushless motors at the knee and ankle joints, series elastic actuators for torque control, and an IMU mounted to the thigh portion to measure residual limb angle.

subjects' gait data used to generate the control surfaces described in ???. For neuromuscular control, we used the black-box CMA-ES optimizer (?) to fit the control parameters as described in (?). For impedance control, we used robust RANSAC linear regression (?) to fit the stiffness, damping, and angle offset parameters within the three discrete phases of stance. The transition between phases 1 and 2 was based on the knee angle crossing a threshold, while the transition between phases 2 and 3 was based on the ankle angle crossing a threshold. We set these thresholds so that 95% of steps in the gait data transition through all three phases. Prior to beginning the experiments, subjects walked with each of the nine control surfaces (parameter sets) for each controller and indicated their preferred settings. All three stance control strategies were paired with the same swing control strategy, in which minimum jerk trajectories for the knee and ankle are generated at toe-off and tracked with PD-feedback combined with a model-based feed forward term as in (?).

In total, we conducted four experiments:

(1) A test of the ability of each control strategy to reproduce a normal walking gait pattern. Able-bodied subjects walked without the use of handrails 0.8 m/s and the amputee subject used the handrails and walked at 0.6 m/s. All subjects walked with their preferred parameters for each controller for one minute. We compared the resulting prosthesis knee and ankle kinematics and kinetics to able-bodied gait data (?) to determine the naturalness of gait.

(2) A comparison of the robustness of the three controllers to ground height disturbances. We simulated a ground disturbance by having subjects step on 3 cm blocks placed on the treadmill. We tested the controllers in a random order in an ABCCBA sequence. In each trial, the subjects stepped on blocks 20 times. We recorded the number of falls, defined as instances when subject needed support from either the handrails or a ceiling mounted harness to regain balance.

(3) A test of the adaptability of the phase estimate. To test the adaptability, we had subjects use the proposed GP-EKF control while the treadmill speed varied sinusoidally between 0.4 and 1.2 m/s with a 20 s period. We compared the phase and phase velocity estimates given by the EKF filter to the true phase, assumed to increase linearly from zero at heel strike to one at toe off, and the true phase velocity, assumed to equal  $1/T_n$ , where  $T_n$  is the duration of the current stance. As a baseline, we compared the EKF to time-based phase and phase velocity estimates, which assume the duration of the current stance will be the same as the previous stance, resulting in the phase

and phase velocity estimates

$$\phi_{\text{time based}} = t_n/T_{n-1} \quad (7.16)$$

$$\dot{\phi}_{\text{time based}} = 1/T_{n-1}, \quad (7.17)$$

where  $t_n$  is the time after heel-strike of the current stance and  $T_{n-1}$  is the duration of the last stance.

(4) Finally, a test of the ability of the GP-EKF control to respond to sudden treadmill stops. If the subject stops his or her gait, then the phase estimate should stabilize and the phase velocity should trend towards zero. The corresponding desired joint angles should approach 5 deg as shown in ??.

We assess significant differences between conditions via the two-sided paired Wilcoxon signed rank test (?). Experienced subject data was not considered for significance testing.

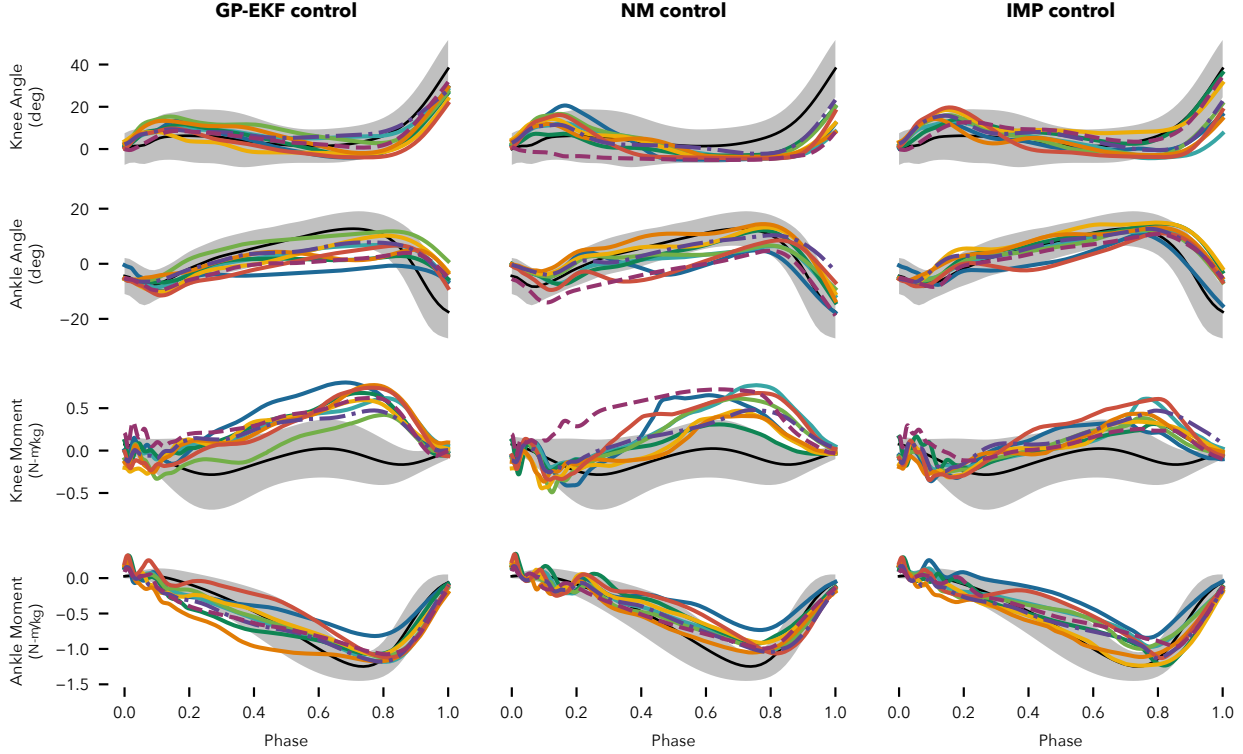


Figure 7.3: Ability to reproduce normal walking. Average knee angle (row 1), ankle angle (row 2), knee moment (row 3), and ankle moment (row 4) for the GP-EKF controller (column 1), neuromuscular controller (column 2), and impedance controller (column 3). Black traces and gray shaded areas show the mean and two standard deviations for very slow human walking data (from (?)). Colored lines show individual subject data. Amputee gait data indicated by dashed lines and experienced user data indicated by dash-dot lines.

### 7.3 Results

#### 7.3.1 Ability to Reproduce Normal Walking

?? shows the average knee and ankle angles as well as the corresponding joint moments generated by the prosthesis controllers during undisturbed walking at 0.8 m/s. All three control strategies produce knee angle trajectories that are similar to the able-bodied data (first row). The neuromuscular (NM) control, however, seems to suffer more from knee over extension during mid-stance and less knee flexion at the end of stance. For some able-bodied subjects, and to a substantial degree for the amputee subject, the knee over-extension causes the joint to engage the mechanical hard-stop on the prosthesis. This triggers a sudden rise in knee torque. ??a summarizes the root-mean-squared (RMS) error between the mean able-bodied knee kinematics and the median knee kinematics of each subject. The GP-EKF control strategy produces significantly more kinematically natural knee angle trajectories, whereas the NM control produces the least kinematically natural knee trajectories.

The second row of ?? shows the average ankle trajectories for each

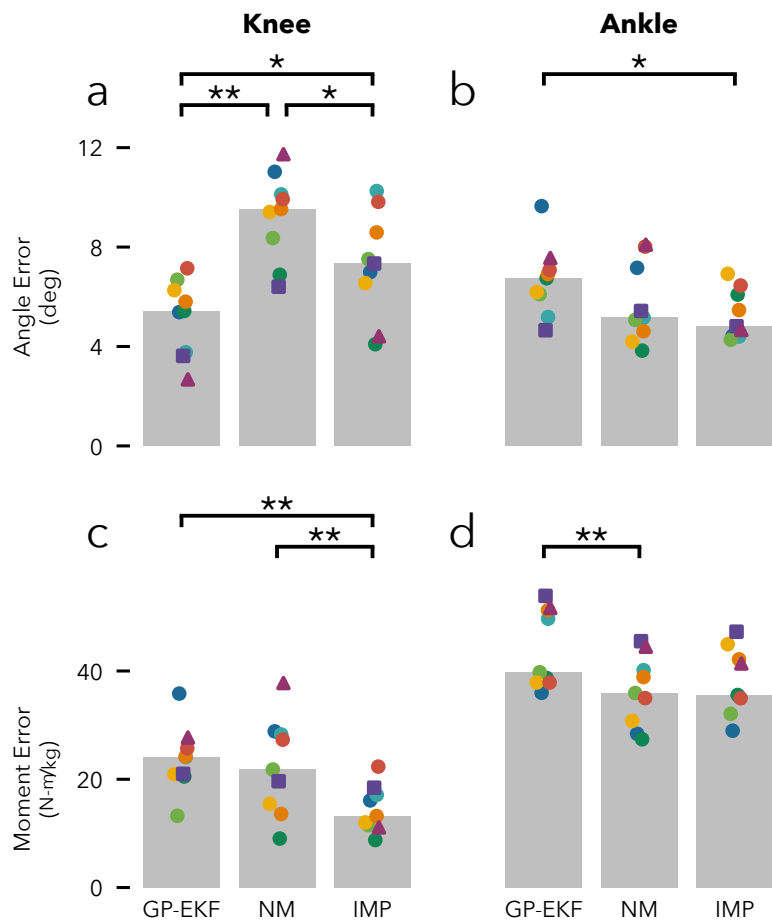


Figure 7.4: Average kinematic (a,b) and kinetic (c,d) errors produced by the three different controllers compared to able-bodied data. GP-EKF produces significantly more natural knee angles than NM or IMP control, but slightly less natural ankle angles and joint torques. Grey bars show median of subject data, circle markers indicate able-bodied subject data, triangle markers indicate amputee data, and square markers indicate experienced able-bodied user data.  
\* :  $p < 0.05$ , \*\* :  $p < 0.01$ .

control strategy. In this case, the GP-EKF control produced the least accurate trajectories. As shown in ??b, this trend reached statistical significance compared to impedance (IMP) control, which produced the most natural ankle angle trajectories. The unnaturalness of the GP-EKF control ankle trajectories is largely due to (1) a lack of plantar flexion in the push-off phase and (2) a lack of dorsiflexion during mid-stance for 3 out of 8 subjects, who all chose the same control surface set.

Finally, the third and fourth row of ?? show the knee and ankle moments for the three controllers. IMP control produced the most natural knee moments by a significant margin (??c), whereas the GP-EKF and NM controllers performed comparably. Although the GP-EKF control produced the least natural ankle moments, the absolute differences were small (??d).

### 7.3.2 Robustness to Ground Height Disturbances

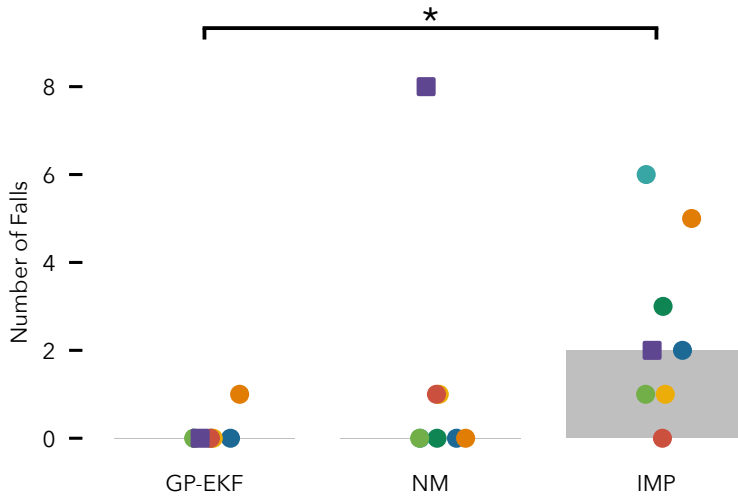


Figure 7.5: Robustness to ground height disturbances. Number of falls accrued for each controller during ground height disturbance trials. GP-EKF control significantly reduced the number of falls compared to IMP control. Grey bars show median of subject data, circle markers indicate able-bodied subject data, and square markers indicate experienced able-bodied user data.  
\* :  $p < 0.05$ .

?? shows the number of times able-bodied subjects fell with each control strategy when stepping on blocks. Subjects fell significantly more often with the IMP control compared to either the GP-EKF or NM controllers. However, when using the neuromuscular control the experienced user fell 8 times, more than any other subject in any condition.

### 7.3.3 Adaptability of Phase Estimate

The adaptability of the phase estimate was tested by sinusoidally varying the treadmill speed during walking. ?? shows the average RMS errors of the EKF-based phase estimate and time-based phase estimate compared to the ground-truth phase obtained in hindsight. For all subjects, the EKF tracked the true phase significantly more accurately than did the time-based phase estimate.

For a more specific example, ?? shows the phase estimates during the treadmill speed variation experiment for a single subject. Because the initial conditions of the EKF and the time-based phase estimates are identical (compare ?? and ??), the phase estimates are similar in early stance. As the treadmill speed changes from one step to the next, the time-based phase estimate diverges significantly from the true phase. The EKF, on the other hand, is able to recover to the true phase towards the end of stance and more accurately predicts the toeoff event.

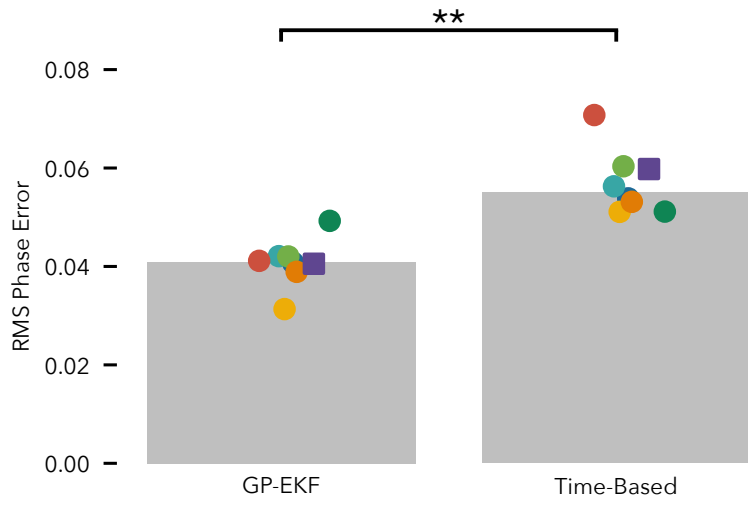


Figure 7.6: Adaptability of phase estimate. Mean phase error of EKF versus time-based phase estimation when walking with sinusoidally varying treadmill speed. The EKF significantly improves phase tracking compared to the time-based estimate. Grey bars show medians of subject data, circle markers indicate able-bodied subject data, and square markers indicate experienced able-bodied user data. \*\*:  $p < 0.01$ .

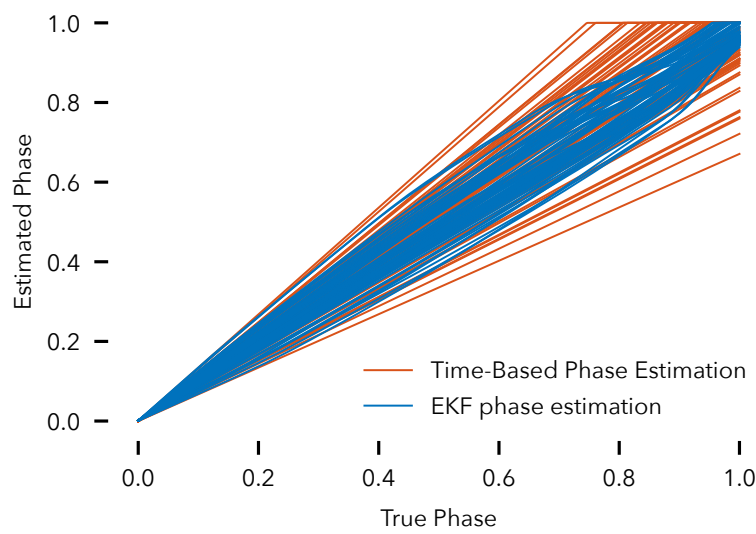


Figure 7.7: Example of EKF-based phase estimation (red) versus time-based phase estimation (blue) for one subject. Due to step-to-step speed variations caused by the sinusoidally varying treadmill speed, the time based phase estimation accrues significant errors. In contrast, the EKF-based phase estimate is able to respond to changes in gait within the gait cycle, thus reducing phase estimation errors.

### 7.3.4 Response to Sudden Treadmill Stops

Finally, ?? shows the phase (a), and phase velocity (b) estimates when the treadmill is suddenly stopped halfway through the stance phase. The EKF phase estimates (solid lines) reflect the fact that the gait cycle has halted, as they do not continue to progress to one. Moreover, when the treadmill stops, the knee (c) and ankle angles (d) approach 5 deg as desired for standing (compare ??). In contrast, the time-based phase estimates (dashed lines in panels (a) and (b)) continue at their initial rate, with the phase reaching one.

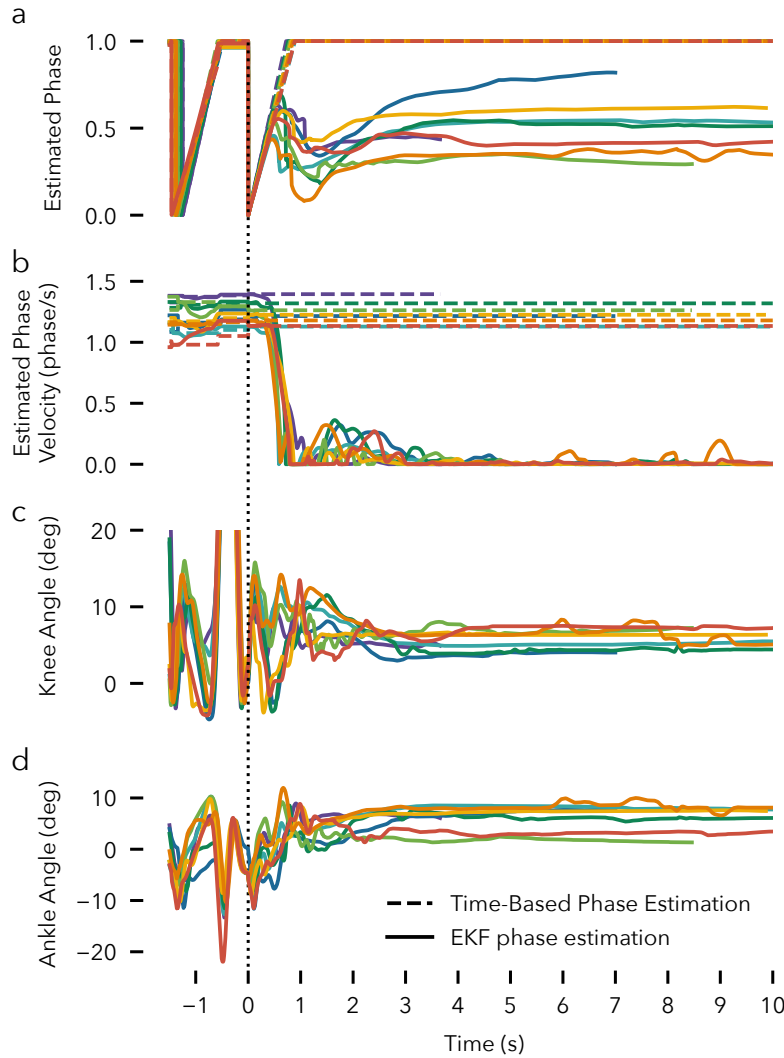


Figure 7.8: Response to sudden treadmill stops. Estimated phase (a) and phase velocity (b), and the measured knee (c) and ankle (d) angles when the treadmill is suddenly stopped half way through stance. When gait stops, the EKF-estimated phase stabilizes to a constant value (solid traces), phase velocity falls to zero, and the joint angles approach 5 deg as desired by the control surfaces (compare ??). The time-based phase estimate fails to respond (dashed lines). Vertical black dotted line indicates heel strike of final stance phase.

#### 7.4 *Discussion*

We proposed a new approach for the control of powered transfemoral prostheses. The approach uses a robust estimate of the gait phase derived from an EKF that integrates multiple sensor measurements to determine the desired knee and ankle angles, velocities and torques from trained control surfaces. The proposed approach improved knee kinematics over NM and IMP control, matched NM control and improves upon IMP control in terms of gait robustness to ground height disturbances, and adapted the phase estimate to both gradual and abrupt changes in speed more quickly than a time-based phase estimate.

We believe the robustness improvements of the proposed GP-EKF control scheme and the NM control over IMP control stem from the smoothness of the phase estimation in these two controllers. In NM control, the phase estimation is implicit and encoded in the internal states of virtual muscles, which are modulated by musculoskeletal dynamics and reflexes. In the proposed control presented here, the EKF directly infers a robust estimate of phase from multiple measurements. In either case, the resulting control commands are smooth and do not normally change abruptly from one moment to the next. In contrast, IMP control splits the stance phase into three discrete phases that are triggered by joint angle thresholds. Consequently, in the ground height disturbance experiments, subjects were occasionally caught off-guard by unexpected transitions, triggered by abnormal kinematics when stepping on a block, which then caused large, sudden changes in torque. Unexpected phase transitions between the mid-stance and late-stance phases were especially consequential, as in the late-stance phase, knee torque trends towards zero to allow for passive knee flexion, while the ankle plantarflexes. If a user's center of mass is positioned incorrectly, this combination of joint torques can cause a sudden collapse of the knee, which was the cause for many of the observed falls with IMP control.

NM control too can result in unexpected falls due to incorrect phase estimation. The experienced user fell a total of eight times when stepping on blocks with the NM control (see square marker ??). These falls were the result of a modelled reflex that reduces knee extensor muscle stimulation in late stance in proportion to ankle plantarflexion, thereby allowing for passive knee flexion leading into swing. In contrast to less experienced subjects, the experienced user was able to control the knee over-extension during stance and achieve more normal knee flexion in late-stance during normal walking (see ?? row 1, column 2). However, this increased knee flexion during normal walking may have increased the prosthesis'

susceptibility to premature knee collapse when disturbed. While the modeled neuromuscular reflexes seem to work well during steady-state walking and during disturbed walking for inexperienced users, the large increase in falls for the experienced user, exposes the difficulty of relying on heuristic reflexes to obtain robust control across a range of gait characteristics. In contrast, the proposed EKF approach takes a principled approach to phase estimation and thus resulted in the fewest falls.

Some improvements can be made in the implementation of the proposed control. First, the normal walking experiments reveal that the ankle trajectories produced by the GP-EKF control are less natural than those produced by NM or IMP control (see ??b). The GP-EKF ankle trajectories in ?? show that peak ankle flexion is achieved later in stance and that the ankle insufficiently plantarflexes at toe-off. These kinematic issues are also present in the desired angles commanded by the GP control surfaces. Therefore, this issue likely stems from a premature cutoff between stance and swing in the gait dataset used to generate the control surfaces. Extending the training data stance duration slightly should increase the desired ankle plantarflexion at the end of stance and engage the peak ankle dorsiflexion earlier.

Second, in the current study, we held constant the impedance about the desired trajectory, represented by  $k_p$  and  $k_d$  in ???. However, recent research has investigated how impedance varies continuously throughout gait (?). These results could be used to parameterize impedance as a function of phase. Taking this step could help improve the naturalness of the knee and ankle torques produced by the GP-EKF controller, which currently trail those produced by the NM and IMP controllers (see figs. ??c and d).

Our work bears some resemblance to the complementary limb motion estimation (CLME) approach proposed by ?. This approach uses linear regression to learn a direct mapping between the angles and velocities of the user's limbs to the prosthesis' joint angles and velocities. There are two key differences between our and the CLME approach. First, our approach only uses signals from sensors mounted to the prosthesis itself, whereas the CLME approach used many IMUs mounted to the torso and sound side leg. Donning these sensors may be impractical for everyday use by an amputee in the real world. Second, the CLME approach directly maps from human to prosthetic joint angles and velocities via linear regression. In contrast, our approach goes through the latent phase and phase velocity states first, which decouples the observation models from the prosthesis control models. This allows us to separately learn the observation models and tune the control models to optimize user preference and

performance.

There are several avenues for future research to expand the proposed control approach. First, we only used prosthesis joint angles and velocities for the observation models. It is worth investigating if additional measurements such as ground reaction forces, accelerations, and EMG signals improve the state estimate. Second, we used a simple, two-state model to represent the entirety of the coupled human-prosthesis state during stance. Adding additional state variables may help capture important behaviors such as balance recovery actions taken by the upper body. To this end, dimensionality reduction techniques could help identify better state representations from gait data. New state representations need to satisfy two constraints that our current model satisfies: (1) The evolution of the state needs to approximately abide by some Markov dynamics model so we can perform the predict step of the EKF (????). (2) The evolution of state throughout stance should be knowable in hindsight after a step is completed so that the observation model can be learned online. Finally, with more advanced state and observation models, more advanced forms of state estimation may be necessary, including unscented Kalman filters or particle filters such as the one proposed by ?, which allows for continuous gait phase estimation using discrete heel and toe contact sensors.

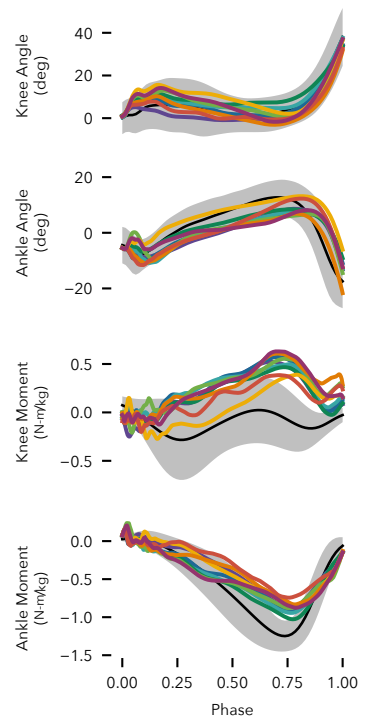


Figure 7.9: GP-EKF phase-based control with fixed control surfaces and increased ankle impedance.

8

## *Future Work*

